HHS Public Access

Author manuscript

Immunity. Author manuscript; available in PMC 2024 March 14.

Published in final edited form as:

Immunity. 2023 March 14; 56(3): 576–591.e10. doi:10.1016/j.immuni.2023.01.032.

Dysregulated tissue niche potentiates resident lymphocytes to suppress an interferon-sensitive stem cell reservoir in emphysema

Chaoqun Wang[1,5], **Benjamin Hyams**[1,2], **Nancy C. Allen**[1,2], **Kelly Cautivo**[3,4], **Kiara Monahan**[1,2], **Minqi Zhou**[1,2], **Madelene W. Dahlgren**[3,4], **Carlos O. Lizama**[2], **Michael Matthay**[1], **Paul Wolters**[1], **Ari B. Molofsky**[3,4,*], **Tien Peng**[1,2,4,6,*]

[1]Department of Medicine, University of California San Francisco, San Francisco, CA 94143, USA

[2]Cardiovascular Institute and Division of Pulmonary, Critical Care, Allergy and Sleep Medicine, University of California San Francisco, San Francisco, CA 94143, USA

[3]Department of Laboratory Medicine, University of California San Francisco, San Francisco, CA 94143, USA

[4]Bakar ImmunoX Initiative, University of California San Francisco, San Francisco, CA 94143, USA

[5]Zhongshan Institute for Drug Discovery, Chinese Academy of Sciences Zhongshan 528400, China

[6]Lead contact

Summary

Aberrant tissue-immune interactions are the hallmark of diverse chronic lung diseases. Here we sought to define these interactions in emphysema, a progressive disease characterized by infectious exacerbations and loss of alveolar epithelium. Single cell analysis of human emphysema lungs revealed the expansion of tissue-resident lymphocytes (TRLs). Murine studies identified a stromal niche for TRLs that expresses *Hhip*, a disease-variant gene downregulated in emphysema. Stromal-specific deletion of *Hhip* induced the topographic expansion of TRLs in the lung that was mediated by a hyperactive hedgehog-IL-7 axis. 3D immune-stem cell organoids and animal models of viral exacerbations demonstrated that expanded TRLs suppressed alveolar stem cell growth through Interferon gamma (IFNγ). Finally, we uncovered an IFN-sensitive subset of human alveolar stem cells that was preferentially lost in emphysema. Thus, we delineate a novel stromal-lymphocyte-epithelial stem cell axis in the lung that is modified by a disease-variant gene and confers host susceptibility to emphysema.

---

[*]Address correspondence to: Ari B. Molofsky, M.D., Ph.D., University of California, San Francisco, 513 Parnassus Ave., HSW Building, Room 1201, San Francisco, CA 94143, ari.molofsky@ucsf.edu; Tien Peng, M.D., University of California, San Francisco, 513 Parnassus Ave., HSE Building, Room 1312, San Francisco, CA 94143, tien.peng@ucsf.edu.

Author Contributions

C.W., A.M., and T.P. conceived the experiments and wrote the manuscript. C.W., B.H., N.C.A, K.M., K.C., M.Z., M.D., C.L., M.M., and P.W. performed the experiments, collected samples, and analyzed data.

The authors declare no competing interests.

Author Manuscript Author Manuscript Author Manuscript Author Manuscript

Author Manuscript Author Manuscript Author Manuscript Author Manuscript

Keywords

Lung; Emphysema; COPD; tissue-resident lymphocytes; stroma; fibroblast; niche; respiratory viral infection; hedgehog; HHIP; Interleukin 7; alveolar stem cell; Interferon gamma; adventitia

Introduction

A fundamental adaptation of barrier epithelia is the ability to host resident immune cells that respond locally to diverse environmental pathogens and insults. In particular, the establishment of lymphocyte residency integrates the innate and adaptive immune response at the barrier, where innate lymphoid cells (ILCs), unconventional T cells, and $CD4^+$ and $CD8^+$ tissue-resident memory T cells (TRMs) are uniquely positioned to act as first-responders to common and repetitive stimuli [1]. While the antimicrobial benefits of these tissue-resident lymphocytes (TRLs) are well-established, the potential cost of their tissue residency to the host organ is less clear. This is particularly relevant in the lung, where the barrier epithelia must not only limit microbial invasion but also allow for efficient gas exchange. Indeed, repetitive infections with air-borne microbes have been linked to the pathogenesis of chronic lung diseases characterized by excessive inflammation such as chronic obstructive pulmonary disease (COPD) [2].

COPD is a highly prevalent and incurable lung disease affecting close to 10% of adults worldwide [3]. COPD represents a spectrum of lung dysfunctions ranging from airway inflammation (chronic bronchitis) to loss of respiratory epithelium (emphysema). The typical clinical course of COPD is characterized by periods of symptomatic stability punctuated by acute exacerbations that lead to stepwise and irreversible declines in lung function [4]. Respiratory tract infections are implicated as the major trigger for acute exacerbations [5]. Thus, resolving the mechanistic link between acute infectious exacerbations and progressive loss of lung function could reveal targeted approaches to treat COPD, moving beyond current treatments with corticosteroids that have broad systemic side-effects and do little to halt long-term disease progression.

The hedgehog interacting protein (*HHIP*) locus has been repeatedly identified in large genome wide association studies as a disease-susceptibility locus for COPD [6,7]. HHIP is an extracellular antagonist of hedgehog ligands [8], which regulates lung stromal - epithelial crosstalk [9]. Consistent with this, murine models of *Hhip* haploinsufficiency develop age-related emphysema, but also lung inflammation [10], providing an important clue that tissue-specific determinants could modify immune cell residence in a nonlymphoid organ to modify organ pathology. Here, we studied how lung stromal-immune niches impact the development of COPD/emphysema. Our experiments demonstrate an unrecognized axis whereby a dysregulated lung stromal niche can support the maladaptive expansion of TRLs in response to respiratory viral infections, highlighting a cost to barrier organs that serve as hosts to abundant TRLs.

Author Manuscript

Author Manuscript

Author Manuscript

Author Manuscript

Results

Expansion of TRLs in lungs of emphysema patients

We isolated cells from COPD patients undergoing lung transplantation with radiographic evidence of severe emphysema, along with age matched control cadaveric donor lungs without prior history of lung disease (Supplementary Table 1) for single cell RNA sequencing (scRNAseq) (publicly available web browser of our cell atlas is on Cellxgene, see Methods for link). The immune population (*PTPRC*/CD45$^+$) constituted the largest major cell lineage isolated from the lung, and we performed clustering focused on the immune lineages (Fig. 1A, S1A,B). The overall fraction of immune cells was increased in the emphysema lung samples (Fig. S1C), which was accompanied by a further relative expansion of T cells (Fig. 1B and 1C), including both CD4$^+$ and CD8$^+$ T cells and a small population of FOXP3$^+$ regulatory T cells (Fig. 1D, Fig. S1D). The majority of T cells isolated from the human lung demonstrated classic markers of tissue residency, including the expression of *CD69*, *CD44*, *ITGAE*, and *IL7R*, and the lack of expression of *SELL* (CD62L), *S1PR1*, and *CCR7* (Fig. 1D, Fig. S1D). The single cell survey demonstrated that emphysema lungs contained increased fractions of TRLs (hereafter referring to CD3$^+$/CD69$^+$/CD44$^+$/SELL$^-$ T cells in the human lung) (Fig. 1E), but not putative circulating lymphocytes (CLs, referring to CD3$^+$/SELL$^+$/CCR7$^+$ T cells in the human lung, Fig. S1E). CD4$^+$ and CD8$^+$ T-cells fractions were both increased in the emphysema lung (Fig. S1F,G).

Differential gene expression (DEG) analysis comparing TRLs in emphysema and control lungs, coupled with Ingenuity Pathway Analysis (IPA), showed pathways enriched in emphysema TRLs relevant to antiviral response (Th1 pathway, Role of PKR in interferon induction) and the establishment of tissue residency and survival (IL-7 signaling) (Fig. 1F). Consistent with this, emphysema TRLs demonstrate increased expression of genes associated with a type 1 (Th1-associated) immune response (Fig. S1H,I, Supplementary Table 2), in addition to *IL7R* which could promote local survival via IL-7 (Fig. 1G). TRLs were the major source of *IFNG* (Fig. 1H) which drives the anti-viral response in tissues [11].

Histologic analysis of CD3$^+$/CD69$^+$ TRLs showed scant TRLs in control lungs, whereas TRLs in emphysema lungs were increased, often appearing in clusters around the airway, as well as in alveolar regions where the density of alveolar epithelial tissue is reduced (Fig. 1I-K). Together, the cellular survey of immune cells in emphysema revealed an expansion of TRLs that appear poised to respond to viral pathogens.

Hedgehog activation induces IL-7 production from fibroblast that drives TRL expansion

We and others have shown that the Gli1$^+$ fibroblasts, a stromal cell subset enriched around larger airways and vessels within the lung adventitia, promotes tissue residency of lymphocytes [12,13]. We generated an inducible deleter mouse to target Gli1$^+$ fibroblasts ($Gli1^{creERT}$:$Rosa^{DTR/tdTomato}$, referred to as Gli1-DTR, Fig. S2A,B) [12,14]. Respiratory infection with inhalation of adenovirus demonstrated increased T cells in the adventitial space at day 7 (Fig. 2A). To define T cells in the lung that are not in direct contact with the pulmonary circulation, we performed intravenous (IV) anti-CD45 labeling just prior to lung harvest to differentiate circulating (IV anti-CD45$^+$/CD3$^+$) from tissue-resident

Author Manuscript Author Manuscript Author Manuscript Author Manuscript

T cells (IV anti-CD45$^-$/CD3$^+$, hereafter referred to as TRLs in murine lungs) (Fig. 2B), which is confirmed by further flow analyses showing significant enrichment of tissue residence markers (CD44$^+$/CD62L$^-$) in the IV CD45$^-$ T cells (Fig. S2C). Respiratory adenoviral infection in wildtype (WT) animals dramatically increased total TRLs and major TRL subsets (Fig. S2D,E). However, deletion of Gli1$^+$ fibroblasts followed by adenoviral infection significantly reduced the number of TRLs in the lung, including anti-viral IFNγ^+ TRLs (Fig. 2C-E). We also found a significant reduction of IL-17A$^+$ TRLs but not IL-4$^+$ or IL-13$^+$ TRLs after Gli1$^+$ fibroblasts deletion (Fig. S2F-H). In contrast, Gli1$^+$ fibroblast deletion did not impact the number of IV anti-CD45$^+$/CD3$^+$ (hereafter referred to as circulating lymphocytes, or CLs) in the lung nor T cells in the mediastinal lymph nodes (Fig. S2I,J). Furthermore, Gli1$^+$ fibroblast deletion did not alter the number of TRLs in the liver, where Gli1$^+$ perivascular fibroblasts have been previously reported (Fig. S2K) [15], nor did it alter other lung resident immune lineages (Fig. S2L). These data suggest that Gli1$^+$ fibroblasts constitute a TRL niche in the lung.

To better define the cellular heterogeneity of Gli1$^+$ fibroblasts, we performed single cell transcriptomic analysis of Gli1$^+$ cells. This revealed previously annotated lung fibroblast clusters[16], with the majority of cells clustered to adventitial (or "universal" 17) fibroblasts, followed by alveolar and peribronchial fibroblasts and a small number of smooth muscle cells (Fig. 2F, S3A). *Il7* was expressed preferentially in the Gli1$^+$ adventitial fibroblasts (Fig. 2G), which was confirmed by RNA *in situ* analysis (Fig. 2H). We previously showed that *Gli1* expression in lung fibroblasts reflects hedgehog (Hh) activation *via* sonic hedgehog (SHH) secreted from the lung epithelium [9,18]. To screen for factors that might be regulated by hedgehog activation in Gli1$^+$ fibroblasts, we performed bulk RNAseq on SHH-stimulated lung fibroblasts *in vitro*, and cross referenced our gene list with an annotated database of bioactive ligands (Fantom 5) [19] followed by DEG analysis (Supplemental Table 3). One of the top ligands activated by SHH was *Il7* (Fig. 2I). qPCR analysis of Gli1$^+$ and Gli1$^-$ fibroblasts confirms a significant enrichment of *Il7* expression in Gli1$^+$ relative to Gli1$^-$ fibroblasts (Fig. S3B,C), and deletion of Gli1$^+$ fibroblasts resulted in a reduction of *Il7*$^+$ fibroblasts (Fig. S3D-F). Both fibroblast subset(s) and lymphatic endothelial cells were previous implicated as IL-7 sources in lymph nodes and tissues [20-22]. Our data showed that lung adventitial niches, including both Gli1$^+$ adventitial fibroblasts and lymphatic endothelium, can produce IL-7.

We found distinct IL-7 receptor (IL7R)-high and IL7R-low T cell populations by flow cytometry, and the overwhelming majority of IL7R-high T cells were TRLs (Fig. 2J,K, S3G,H). To functionally test the effect of Hh activation on lung fibroblasts and their ability to support TRLs, we cultured TRLs from the uninfected lungs with conditioned media from lung fibroblasts (Fig. 2L). Conditioned media from lung fibroblasts stimulated with SHH *in vitro* significantly increased the number of TRLs in culture, and this effect was blocked by a neutralizing antibody to IL-7 (Fig. 2M). In contrast, TRLs stimulated with SHH in the absence of lung fibroblasts did not expand relative to vehicle control (Fig. S3I).

Author Manuscript Author Manuscript Author Manuscript Author Manuscript

HHIP downregulates the stromal hedgehog-IL7 axis to attenuate TRL expansion

Our single cell analysis of Gli1$^+$ fibroblasts demonstrated a subpopulation of fibroblasts characterized by high *Hhip* expression that was previously annotated as “peribronchial” fibroblasts [16,17], and localized within the broader lung adventitia surrounding the airways but not blood vessels (Fig. 3A-C). RNA *in situ* confirmed the enriched *Hhip* expression that overlaps with Gli1$^+$ fibroblasts around the airway (Fig. 3D). qPCR analysis of lung fibroblasts demonstrated that SHH activates *Hhip* expression (Fig. S4A), and addition of recombinant HHIP to SHH-stimulated fibroblasts abrogates Hh activation and *Il7* induction (Fig. S4B). Addition of HHIP to lung fibroblasts stimulated with SHH also abrogated the ability of the conditioned media to induce TRL proliferation (Fig. S4C). This suggests that secretion of HHIP, an extracellular antagonist of SHH, particularly by peribronchial fibroblasts, can attenuate the stromal TRL niche by downregulating the ability of SHH to induce IL-7 in adjacent adventitial fibroblasts.

To assess the functional role of HHIP in fibroblasts, we generated a *Hhip* flox allele in mice (Fig. S4D) to create $Gli1^{creERT}{:}Hhip^{flox/flox}$ (hereafter referred to as $Gli1^{HHIPCKO}$) animals. Using this tool, we set out to define the topographic localization of TRLs in $Gli1^{HHIPCKO}$ animals by imaging thick lung sections. In control naïve lungs, the majority of TRLs (IV anti-CD45$^-$/CD3$^+$) localized within the adventitial space, with a small minority out in the alveolar compartment (Fig. 3E,F, Fig. S4E). However, *Hhip* deletion in Gli1$^+$ fibroblasts resulted in a significant increase in total number of T cells (Fig. 3E,F). Similar to lungs of patients with emphysema, there was a significant increase in the number of alveolar TRLs in tamoxifen-treated $Gli1^{HHIPCKO}$ lungs compared to controls (Fig. 3F). In contrast, *Hhip* deletion in Gli1$^+$ fibroblasts did not increase CLs (IV anti-CD45$^+$/CD3$^+$) in the lung (Fig. 3G). These results suggest HHIP limits not only lung TRL accumulation but also topographic dispersal to distal lung regions in proximity to alveolar epithelium that participates in gas exchange.

To better define the T cell subsets increased with HHIP deletion, we next performed flow cytometry analysis $Gli1^{HHIPCKO}$ lungs, which confirmed a significant increase in total TRLs (Fig. 3H). Conversely, there was no change in CLs (Fig. S4F). Cytokine analysis demonstrated an increase in IL-17A$^+$ TRLs but not IL-13$^+$ TRLs with *Hhip* deletion (Fig. S4G). Administration of FTY720, an inhibitor of lymphocyte egress, significantly suppressed CLs in the lungs of $Gli1^{HHIPCKO}$ animals (Fig. S4H) but the TRL population remained stable during two weeks of FTY720 administration relative to vehicle (Fig. S4I). TRLs in $Gli1^{HHIPCKO}$ lungs were sometimes localized adjacent to B cells, both scattered and within clusters in the adventitia (Fig. S5A), that resembles bronchus-associated lymphoid tissue (BALT) reported in emphysema lungs [23].

We then performed scRNAseq of TRLs isolated from $Gli1^{HHIPCKO}$ and control lungs. Gene expression analysis confirmed that TRLs expressed residency markers and lacked circulating markers (Fig. 3I, and S5B). While the proportions of TRL subsets did not change with HHIP deletion (Fig. S5C), there was an increase in proliferating TRLs on scRNAseq (Fig. S5D,E). Cell-cell signaling analysis NicheNet [24] to analyze our scRNAseq datasets of TRLs and Gli1$^+$ fibroblasts demonstrated that IL-7/IL7R interaction between fibroblast and TRLs was one of the highest ranked pairings (Fig. 3J). qPCR of lung fibroblasts isolated from

Gli1^{HHIPCKO} confirmed knockdown of *Hhip*, along with induction of *Gli1* and *Il7* (Fig. S5F). We also generated a complementary conditional knockout model that induced a more complete knockdown of *Hhip* (*Ubc*^{creERT}*:Myh11*^{creERT}*:Hhip*$^{flox/flox}$, hereafter referred to as *UM*^{HHIPCKO}), which demonstrated a more robust induction of *Il7* in the lung fibroblasts compared to *Gli1*^{HHIPCKO} (Fig. S5G). Bulk RNAseq of lung fibroblasts from *UM*^{HHIPCKO} animals confirmed induction of *Gli1* and *Il7*, along with knockdown of *Hhip* (Fig. S5H). DEG analysis showed an induction of *Il12b*, another T cell mitogen and activation factor [25], was also upregulated in lung fibroblasts activated with SHH (Supplementary Table 3). Recombinant IL-7 and IL-12 both enhanced TRL survival in culture in the absence of T-cell receptor stimulation and other survival factors, although IL-7 was more potent than IL-12 (Fig. S5I). These data demonstrated that HHIP, a gene associated with susceptibility to emphysema, modifies the stromal niche to limit TRLs in the lung during homeostasis.

HHIP loss exacerbates TRL expansion and emphysema after viral infection

To examine the effect of HHIP on the inflammatory reaction after viral challenge, we administered tamoxifen or vehicle to *Gli1*^{HHIPCKO} animals followed by repetitive adenoviral challenges. In the control lungs, there were few CD3$^+$/CD44$^+$ TRLs in the alveoli (Fig. 4A). Tamoxifen induction of *Hhip* deletion alone or adenoviral infections alone both increased the number of TRLs in the alveoli, but *Hhip* deletion combined with adenoviral challenge showed the most significant expansion of lung TRLs (Fig. 4A,B). Flow cytometry also confirmed the expansion of TRLs in the lung (Fig. S6A).

Next, we examined the effect of viral exacerbation on lung structure. Control lungs without viral infection exhibited small alveolar space with limited distances between alveolar walls, indicative of a highly sacculated network of gas exchange surfaces (Fig. 4C). *Hhip* deletion from Gli1$^+$ fibroblasts alone induced mild emphysematous changes, indicated by an enlargement of alveolar space quantified by the mean linear intercept (MLI) between alveolar walls. However, *Hhip* deletion followed by adenoviral challenge resulted in the most alveolar simplification and airspace enlargement, reminiscent of patients with emphysema (Fig. 4C,D). To quantify the alveolar changes in a manner consistent with clinical studies of emphysema patients, we also performed computed tomography (CT) quantification of alveolar destruction marked by percentage of low attenuation areas (%LAA). *Hhip* deletion with adenoviral infection resulted in increased %LAA on CT of the lungs compared to adenoviral infection alone or uninfected controls (Fig. S6B,C). We did not observe changed elastin staining (Fig. S6D) or alterations of the expression of proteases known to cleave elastin in the lung fibroblasts of *UM*^{HHIPCKO} animals (Supplementary Table 4).

The alveolus is populated with alveolar epithelial type 2 cells (AT2s) that produce surfactant and serve as the stem cell reservoir for the alveolar epithelial surface [26]. Quantification of AT2 density in the lung revealed an inverse correlation with airspace enlargement (MLI) in the viral challenged lungs, with the most significant loss of AT2s seen in *Gli1*^{HHIPCKO} lungs followed by adenovirus challenge (Fig, 4E, F). These experiments show that loss of HHIP in the stroma potentiates TRL expansion after viral infection concurrent with loss of a resident stem cell pool.

Author Manuscript Author Manuscript Author Manuscript Author Manuscript

Author Manuscript

IFNγ drives emphysematous changes after viral exacerbation

TRLs are the main source of IFNγ, a canonical Th1 cytokine that is critical for anti-viral immunity (Fig. 1H). To determine whether excess IFNγ is sufficient to induce emphysema, we utilized a genetic model where IFNγ is over-produced in lymphocytes (YFP enhanced transcript for *Ifng*, hereafter referred to as YETI)[27](Fig. S6E). Bulk RNAseq of fibroblasts isolated from $\text{YETI}^{\text{YFP/+}}$ and control lungs demonstrated significant induction of IFN-responsive genes in the YETI/+ lung fibroblasts (Fig. S6F). $\text{YETI}^{\text{YFP/+}}$ animals developed spontaneous emphysematous changes at 3 months of age compared to WT littermates (Fig. 5A,B), which was accompanied by a loss of AT2s in the alveoli of $\text{YETI}^{\text{YFP/+}}$ animals (Fig. 5C,D).

To determine whether lung TRLs can directly suppress AT2 growth *ex vivo*, we developed a TRL-AT2 organoid platform (Fig. 5E). AT2s (SFTPC Lin^+, or tdtomato^+) were sorted from healthy $Sftpc^{creERT}$:$Rosa^{tdtomato}$ animals after tamoxifen induction and implanted in matrigel droplets where they can form 3D organoids. In the same well as the AT2 organoids, we isolated TRLs from the same lungs in the media outside of the matrigel droplet, so that the TRLs are not in physical contact with the AT2s but are able to participate in paracrine interactions. In this setup, AT2s cultured alone in a feeder-free media supplemented with IL-2, IL-12, and IL-18 were able to expand appropriately and form organoids (Fig. 5E). However, co-culture with TRLs significantly suppressed AT2 organoid growth (Fig. 5E-G). Addition of recombinant IFNγ to AT2 organoids demonstrated a significant defect in AT2 growth without a change in the proportion of KRT8+ cells previously described as transitional cell types [28-30] (Fig. S6G-K). Finally, addition of a neutralizing anti-IFNγ antibody to the TRL-AT2 organoids partially rescued the AT2 growth defect attributed to TRLs (Fig. 5E-G).

To test whether IFNγ blockade can rescue AT2 loss in our model of COPD acute exacerbation *in vivo*, we administered a weekly dose of anti-IFNγ or isotype IgG into our $Gli1^{HHIPCKO}$ animals challenged with adenoviral infections. Histologic assessment of alveolar morphometry revealed that anti-IFNγ treated animals had reduced alveolar space enlargement and increased AT2s (Fig. 5 H-K). Finally, we performed an identical rescue experiment using anti-IL7R previously reported to limit tissue resident T cells [31,32], and we were able to rescue the emphysematous phenotype seen in our viral exacerbation model (Fig. S6L,M). Together, these data suggest IFNγ secreted from TRLs is both necessary and sufficient to drive emphysematous changes in our murine models.

An Interferon-poised CD66c^+ AT2 subset is lost in COPD/emphysema lungs

Single cell analysis of the non-immune fraction of the lung cells isolated from emphysema and control patients demonstrated a large reduction of epithelial and endothelial cells in the diseased state (Fig. 6A,B, S7A), which accurately reflects the dramatic loss of gas exchange surface in emphysema. Within the non-immune lineages, AT2 cells demonstrated the most dramatic loss in emphysema (Fig. 6C). Subcluster analysis revealed two distinct human AT2 subsets (Fig. 6D, S7B), consistent with a recent single cell atlas of the healthy human lung that highlighted AT2 heterogeneity[33]. The previously published human lung cell atlas demonstrated a small subset of AT2s with enriched Wnt-signaling (termed “AT2-signaling”)

Author Manuscript

Author Manuscript

Author Manuscript

Author Manuscript

relative to the rest of the AT2 population (termed “AT2-bulk”), with unclear functional implications for human lung regeneration. DEG analysis between the two subsets found that *CEACAM6* (CD66c) was highly enriched in the AT2-signaling population (Fig. 6E, Fig. S7B Supplementary Table 5). CD66c$^+$ AT2s have similar transcriptomes compared to a previously described AT2 subset found near the respiratory bronchioles (RB, SCGB3A2$^+$ cells at the airway termini) in the human lung [34,35], but we did not note a preferential localization of CD66c$^+$ AT2s to RBs (Fig. S7C). In contrast to mouse lungs, human lung *HHIP* is predominantly expressed in the CD66c$^-$ AT2s (Fig. S7B), which demonstrated reduced *HHIP* expression in emphysema compared to controls (Fig. S7D). When we further compared the relative proportion of AT2 subsets in emphysema vs. control human lungs, we uncovered a loss of the CD66c$^+$ AT2s relative to CD66c$^-$ AT2s in emphysema (Fig. 6F,G), which is confirmed on histologic analysis of emphysema vs. controls lungs (Fig. 6H,I).

To examine upstream regulators that might shed light on differences between the two AT2 subsets, we performed IPA analysis of the DEGs (CD66c$^+$ vs. CD66c$^-$). The top 3 upstream regulator gene pathways activated in CD66c$^+$ AT2s are MYC, MYCN, and IFNG (Fig. 6J). JAK/STAT signaling downstream of IFNG was also activated on the IPA (Fig. S7E). Of note, the top upstream regulator activated in CD66c− AT2s (suppressed in CD66c$^+$ AT2s) is ETV5 (Fig. 6J), a master regulator of AT2 maturation and surfactant production, which is the primary function of differentiated AT2s. Consistent with the IPA analysis, DEGs demonstrated increased expression of both *IFNGR1* and *IFNGR2* in CD66c$^+$ AT2s along with other IFN response genes (Fig. 6K). In contrast, CD66c$^-$ AT2s are enriched in expression of genes relevant to surfactant production driven by ETV5, including *SFTPA1, SFTPA2, SFTPC, LAMP3*, and *ABCA3*. (Fig. 6K). This suggests that human emphysema lungs are characterized by the loss of a specific subset of alveolar stem cell (CD66c$^+$ AT2) that appears more progenitor-like and poised to respond to IFNγ signaling.

CD66c$^+$ AT2s constitute an IFN-sensitive stem cell reservoir suppressed by TRLs

To functionally validate the IPA analysis, we sorted AT2 cells from healthy human lungs (EpCAM$^+$/HTII-280$^+$) and utilized anti-CD66c to compare CD66c$^+$ vs. CD66c$^-$ AT2s for organoid assays (Fig. 7A). CD66c$^+$ AT2 organoids demonstrated significantly higher clonogenic capacity compared to CD66c$^-$ AT2s when cultured in previously defined growth media for human AT2s [36] (Fig. 7B,C). Addition of Wnt3a and R-spondin1 (RSPO1) augmented the proliferation of CD66c$^+$ AT2s but not CD66c$^-$ AT2s (Fig. S7F), Furthermore, Wnt target genes are enriched in CD66c$^+$ AT2s (Fig. 7D), suggesting that CD66c$^+$ AT2s constitute a stem cell subset that is more receptive to Wnt activation, which suggests homology of human CD66c$^+$ AT2 subset with murine Wnt-active AT2 subset that had been demonstrated to be highly proliferative [37,38].

To test the effect of IFNγ on the two AT2 subsets, we treated CD66c$^+$ and CD66c$^-$ organoids with recombinant IFNγ. qPCR analysis demonstrated that CD66c$^+$ AT2s had elevated basal levels of IFNγ target gene expression. Upon IFNγ induction, CD66c$^+$ AT2s demonstrated significantly higher absolute induction of IFNγ target genes relative to CD66c$^-$ AT2s (Fig. 7E). Furthermore, IFNγ attenuated Wnt target genes in CD66c$^+$ AT2s (Fig. 7D). Consistent with the exaggerated IFNγ response exhibited by CD66c$^+$

Author Manuscript Author Manuscript Author Manuscript Author Manuscript

AT2s, escalating concentrations of IFNγ produced a dose-dependent inhibition of CD66c$^+$ AT2 proliferation (Fig. 7F,G). In contrast, similar dose range of IFNγ had minimal effect on CD66c$^-$ AT2 proliferation (Fig. 7F,G). Together, these findings suggest CD66c$^+$ AT2s represent a novel stem cell reservoir defined by sensitivity to IFNγ-mediated growth suppression in part by attenuating Wnt activation.

To functionally test the effect of human lung TRLs on CD66c$^+$ AT2s, we devised an immune-AT2 heterotypic organoid platform where the epithelial stem cells are cultured in matrigel on an air-liquid interface above the transwell and TRLs are cultured below. Human TRLs were isolated using a flow cytometry panel that was found to identify tissue resident T cells in the human lung when perfused with IV anti-CD45 under *ex vivo* lung perfusion (CD45$^+$/CD3$^+$/CD56$^-$/CD69$^+$/CD44$^+$/CD62L$^-$) [39]. The source of the TRLs and AT2s were from the same donor, and the autologous TRLs and CD66c$^+$ AT2s were not in direct physical contact. Co-culture of TRLs with CD66c$^+$ AT2s led to a significant reduction in organoid growth. Furthermore, the introduction of a neutralizing anti-IFNγ antibody rescued the attenuation of CD66c$^+$ AT2 growth by TRLs (Fig. 7H,I). We conclude that human IFNγ-producing TRLs are sufficient to suppress CD66c$^+$ AT2 proliferation *in vitro*.

Discussion

The respiratory tract constitutes the largest barrier surface in the human body and is the portal of entry for air-borne particles and microbes, including pathogens such as common and novel respiratory viruses. It must provide a suitable niche for tissue-resident immune cells that can limit infection at the lung barrier, but at what cost to the host? The immune system is equipped with multiple leukocyte-mediated autocrine and paracrine counter-regulatory mechanisms that limit excessive immune cell residency and activation. However, tissue-specific susceptibilities that predispose to excessive organ inflammation and long-term damage are not well defined. Our study highlights the stroma in nonlymphoid organs as a critical nexus for lymphocyte tissue-residency that can modify disease phenotypes such as chronic lung inflammation and loss of gas exchange surface seen in COPD/emphysema. The role of HHIP in this tissue circuit also demonstrates how disease-associated variants can offer both beneficial and pathologic consequences (*i.e.* antagonistic pleiotropy) to the host organ, where loss of HHIP may increase antiviral defense by potentiating local IFNγ-secreting TRLs, but also predisposes to further loss of alveolar stem cells that make up the gas-exchange surface. These studies highlight a mechanism where excessive TRLs can promote the decline of lung function and offer therapeutic targets to counter the tissue-suppressive effects of TRLs in COPD/emphysema.

Here our data show that Gli1$^+$ fibroblasts in the adventitia are tightly regulated by SHH, including a negative feedback loop mediated by HHIP, which impacts their production of the lymphocyte supporting signal IL-7, and ultimately regulates the magnitude of lymphocyte residence at rest and particularly after viral inflammatory insults. In addition, adventitial spaces are enriched for TSLP, IL-33, prostanoids, and diverse chemokines that may also contribute to our observations [40]. Of note, we find that a dysregulated adventitial niche due to loss of HHIP is associated not just with increased lymphocytes but also a dispersal of TRLs into distal alveolar regions, a zone dominated by CLs rather than TRLs in healthy

Author Manuscript Author Manuscript Author Manuscript Author Manuscript

lungs. This redistribution may be adaptive in the setting of acute infections. However, it also has negative consequences, repressing alveolar epithelial cells and their restorative capacity and driving an emphysema like phenotype in mice over time (and genetic risk for development of emphysema in humans). Whereas *Hhip* is most highly expressed in peribronchial fibroblasts in mouse, the human orthologue (*HHIP*) is predominantly expressed in the alveolar epithelium (preferentially in CD66c$^-$ AT2s). The increased presence of HHIP in the human alveolus suggests a crucial species-specific requirement to suppress hedgehog signaling in the gas exchange surface, which correlates with primate lungs that are larger with more complex airway architecture. This also supports the role of HHIP in restricting TRL residency in the human alveolus. Together, adventitial niches may serve both as critical immune hubs and safeguards that restrict excessive lymphocyte dispersal and damage to critical epithelial progenitor pools.

AT2s represent a classic example of the importance of facultative progenitors in the lung, where they provide both a stem cell reservoir and a specialized role in organ function. A recent single cell atlas of the human lung described two distinct AT2 subsets[33], one enriched in Wnt-response genes and the other enriched in genes associated with surfactant synthesis [41]. While this single cell study poses intriguing questions about functional differences between human AT2 subsets, it has not been experimentally tested. Taking advantage of our cell surface marker analysis, we found that CD66c$^+$ AT2s exhibit increased clonogenicity when cultured in a media condition containing Wnt agonist, which supports their potential role as the progenitor AT2 reservoir. This suggests that the human AT2s have evolved and bifurcated to take on more specialized functions, with CD66c$^+$ AT2s providing a stem cell reservoir and CD66c$^-$ AT2s maintaining surfactant production within the alveoli.

Teleologically, it makes sense that a more proliferative stem cell reservoir would also be more sensitive to a cell-mediated immune response that serves to attenuate viral replication. IFNs act by recruiting and activating immune cells while also upregulating antiviral response in both infected cells and their neighbors [42]. Here we demonstrate that one of those antiviral responses is to suppress the proliferation of a unique lung epithelial progenitor population. Numerous respiratory viruses, including the recently identified SARS-nCOV2, display tropism for AT2[36], and suppressing the proliferation of infected AT2s would be a vital component of the host-pathogen interaction to contain viral replication. However, herein lies the cost to the organ if excessive tissue residency is granted to IFN-expressing lymphocytes. In our study, we made a surprising observation that CD66c$^+$ AT2s were enriched in genes necessary for an interferon response, even in the non-diseased lungs. We demonstrated that the lung contains a specialized stem cell reservoir that is primed for IFN-mediated antiviral response, and numerical and topographic expansion of IFNγ^+ TRLs in the lung leads to the loss of a more regenerative AT2 progenitor subset required to replete the alveoli.

Prior histologic analysis of COPD/emphysema lungs show a direct correlation with T cell abundance (particularly CD8$^+$ T cells) and emphysema severity [43], but how T cells might mediate the emphysematous phenotype is unclear. One hypothesis is that T cells promote emphysema through the secretion of inflammatory cytokines that upregulates proteases which degrade the matrix of the alveoli [44]. Our TRL-AT2 organoid assays demonstrated that IFNγ directly suppressed AT2s, independent of matricellular changes. Furthermore, it

Author Manuscript
Author Manuscript
Author Manuscript
Author Manuscript

outlines a direct interaction between T cells and a stem cell pool that repletes the functional gas exchange surface of the lung. Probing the interaction between TRLs and AT2s could reveal potential new targets for COPD/emphysema. Our studies highlighted altered stromal niches as additional potential targets for therapeutics. Inhaled or systemic corticosteroids are the current standard therapy for COPD, but their effects are broad with unclear effects on TRLs in the lung. Corticosteroids preferentially suppress CD4$^+$ T cells, while CD8$^+$ T cells are relatively resistant [45]. Our studies suggest that more tailored therapies are possible to directly target TRLs in the lung that could drive tissue loss and functional decline in COPD.

Limitations of the Study:

Our study raises several critical and unanswered questions. (1) Loss of stromal cell HHIP expression is associated with increased mouse lung TRLs, predominantly of the type 3/17 subset. However, with concurrent viral challenge, or after aging mice, we find type 1 IFNγ^+ lymphocytes further increase, including CD8$^+$ T cells, which are also more dispersed in alveolar regions. Volumetric imaging does not reveal an overt topographic ‘dispersal’ of Gli1$^+$ fibroblasts, although they remain associated with a range of increased lymphocyte and lymphoid structures, dominantly in the lung adventitial regions. Increased production of IL-7 or related signals in adventitial niches could lead to elevated alveolar interstitial concentrations and underlie this type 1 lymphocyte ‘alveolar-dispersal’, although other possibilities remain. (2) Gli1 expression extends to adventitial fibroblast (AF) subsets in multiple tissues; although our data did not identify a systemic impact of AF-like (Gli1$^+$) cell deletion, these remain possible. (3) Our data suggest a tissue-resident phenotype for lung lymphocytes in our systems, supported by transcriptomic analysis, trafficking blockade (FTY-720), and intravascular labeling. However, as tissue residency is a spectrum of states, it remains likely that blood derived lymphocytes contribute to our phenotypes over time. Clearly, future work will be required to understand these questions, including the possible role of lymphocytes recruited from circulation.

STAR★METHODS

RESOURCE AVAILABILITY

Lead Contact—Further information and requests for resources and reagents should be directed to and will be fulfilled by the Lead Contact, Dr. Tien Peng (Tien.peng@ucsf.edu).

Materials Availability—The *Hhip*$^{flox/flox}$ conditional knockout mouse line was generated in this study. Request for this line will be fulfilled by Dr. Tien Peng.

Data and Code Availability—The sequencing data reported in this study are deposited in NCBI Gene Expression Omnibus (GEO) under the accession number: GSE196638, GSE206721, GSE209734, and GSE209735 The Gli1+ fibroblats scRNAseq data were previously deposited in GEO (GSE140032). The single cell atlas of emphysema described in this manuscript can be visualized on https://cellxgene.cziscience.com/collections/03cdc7f4-bd08-49d0-a395-4487c0e5a168/private?explainNewTab

Author Manuscript

Author Manuscript

Author Manuscript

Author Manuscript

EXPERIMENTAL MODEL AND SUBJECT DETAILS

Human Lung Samples—Studies involving human tissue were approved by the UCSF Institutional Review Board. All subjects provided written informed consent. Peripheral regions of the normal lungs were obtained to select for the distal regions of the lung from brain-dead donors that were rejected for lung transplantation. COPD/emphysema lung specimens were taken from the patients undergoing lung transplantation for COPD with radiographic evidence of severe emphysema.

Animal Studies—All mice were housed and treated in accordance with the IACUC protocol approved at the University of California, San Francisco. Mice between the ages of 8-12 weeks old were used for the experiments and littermates were used as controls with balance of gender between groups. C57BL/6 mice were obtained from Jackson Laboratory. The generation and genotyping of the $Gli1^{creERT2}$, $R26R^{EYFP}$, $R26R^{tdTomato}$, $R26R^{DTR}$, $Ubc^{creERT2}$ and $Myh11^{creERT2}$ lines were performed as previously described by The Jackson Laboratory. Generation and genotyping of the $Sftpc^{creERT2}$[46] and $Yeti^{YFP}$[27] lines were performed as previously described. The $Hhip^{flox/flox}$ line was generated in our lab, and genotyping primers are listed in KEY RESOURCES TABLE.

METHOD DETAILS

Tamoxifen, Adenovirus, Diphtheria Toxin, FTY720, and Antibody Administration—Tamoxifen (Sigma) was dissolved in corn oil (Sigma) and administered intraperitoneally at 200 mg/kg per day x 3-5 days for lineage labelling and gene deleting studies. For viral infection, adenoviruses (WC-U of Iowa-272) were suspended in PBS and administered intranasally at $1X10^8$ or $1X10^9$ PFU/animal. For depleting Gli1+ cells *in vivo*, diphtheria toxin (Sigma) was administered intraperitoneally at 50 ng/g of mouse per day x 5 days. For FTY720 treatment, FTY720 was administered intraperitoneally at 3 mg/kg of mouse every two day for 7 doses. For blocking IFNγ in mice, anti-mouse IFNγ (XMG1.2, BioXCell) or IgG isotype control (BioXCell) were administered intranasally at 100 µg/dose weekly per animal for 7 doses. For depletion of T cells in vivo, anti-mouse IL7R (BioXCell) or IgG isotype control (BioXCell) were administered intranasally at 100 µg/dose weekly per animal for 7 doses. At indicated time points, lungs were collected for flow cytometry or histological analysis.

Tissue Dissociation and Flow Cytometry—Dissected mouse lung was tracheally perfused with a digestion cocktail of Collagenase Type I (225 U/ml, Thermo Fisher), Dispase (15 U/ml, Thermo Fisher) and Dnase (50 U/ml, Sigma) and removed from the chest. For FACS analysis of immune cells, a digestion cocktail of Liberase TM (100 µg/mL, Sigma) and Dnase (50 U/ml, Sigma) in HBSS was used to dissociate the lung. The lung was further diced with razor blades and the mixture was incubated for 45 mins at 37 °C and vortexed intermittently. The mixture was then washed with FACS buffer (2% FBS in DMEM-F12). The mixture was passed through a 70 µm cell strainer and resuspended in RBC lysis buffer, before passing through a 40 µm cell strainer. For liver, whole organs were excised, cut in small pieces with an automated tissue dissociator (GentleMacs; Miltenyi Biotec) and then digested in 1X HBSS with 0.2 mg/mL Liberase Tm, 25 mg/mL DNase, 0.5% BSA for 30 mins at 37 °C on a shaker. Samples were

Author Manuscript Author Manuscript Author Manuscript Author Manuscript

subsequently processed on the GentleMacs again, followed by filtration through 70 μm filters, washed, and subjected to red blood cell lysis before final suspension in FACS buffer. Liver samples were spun to remove hepatocytes then further separated using 40% Percoll-HBSS gradient (GE Healthcare #17-0891-01) and centrifugation (1400 x g, 20 mins, room temperature, no brake). Lymph nodes were prepared by mashing tissue through 70 μm filters without tissue digestion, followed by centrifugation and red cells lysis steps. Cells suspensions were incubated with the appropriate antibodies in FACS buffer for 30 min at 4°C and washed with FACS buffer. The following antibodies were used for staining: CD45-BV421 (BD, 563890), CD45-BUV395 (BD, 564279), CD11b-BV605 (BD, 563015), CD3e-APC (Biolegend, 100312), CD3e-Alexa Fluor700 (Biolegend, 100216), CD4-BV711 (Biolegend, 100549), CD8a-PE (Biolegend, 100707), CD8a-FITC (Biolegend, 100705), CD19-PE/Dazzle 594 (Biolegend, 115554), NK-1.1-BV650 (Biolegend, 108736), CD44-BV785 (Biolegend, 103041), CD62L-PE (Biolegend, 104407), IFN-γ-APC (Biolegend, 505810), IL7R-Alexa Fluor647 (Biolegend, 135020), EpCAM-BV421 (Thermo Fisher, BDB563214), CD31-PerCP-eFluor 710 (Thermo Fisher, 46-0311-80), LY6A-APC-Cy7 (Biolegend, 108126), and PDGFRα-APC (Thermo Fisher, 17-1401-81). For distinguishing the resident and circulating lymphocytes, 3 min before euthanizing each mouse, 3 μg of anti-mouse fluorophore-conjugated CD45 antibody diluted in 150 μl of 1X DPBS was intravenously injected via the tail vein or through retro-orbital injections. Cells counts were performed using a NucleoCounter (Chemometic). For experiment involving intra-cellular staining, cells were fixed and permeabilized using Foxp3 Staining Buffer Set (eBioscience). For cytokine production, 2-3x10^6 cells were plated in 96-well U-bottom plate and stimulated ex vivo with 1X Stimulation Cocktail (Tonbo Biosciences) and 1X Brefeldin A Solution (Bioscience) in complete media (RPMI1640 supplemented with 1 mM nonessential amino acids, 2 mM glutamine, 1 mM sodium pyruvate, 100 U/mL penicillin/streptomycin (PS) and 50 μM β-mercaptoethanol) for 3 hours at 37°C.

For human lung, a distal piece of it (~10 cm^3) was dissected from the whole lung and washed with HBSS X 4 times in 15 min. The piece of lung was further diced with razor blades and was added into the digestion cocktail of Collagenase Type I (225 U/ml, Thermo Fisher), Dispase (15 U/ml, Thermo Fisher) and Dnase (100 U/ml, Sigma). The mixture was incubated for 2 h at 37°C and vortexed intermittently. The mixture was then liquefied with a blender and passed through 4X4 gauze, a 100 μm and a 70 μm cell strainer. The mixture was resuspended in RBC lysis buffer, before passing through a 40 μm cell strainer. Cells suspensions were incubated with the appropriate antibodies in FACS buffer for 30 min at 4°C and washed with FACS buffer. The following antibodies were used for staining: CD45-APC-Cy7 (BioLegend, 3304014), CD45-Alexa Fluor488 (BioLegend, 304019), CD31-APC-Cy7 (BioLegend, 303120-BL), CD11b-APC-Cy7 (BD Biosciences, 557754), CD69-BV421 (BioLegend, 310929), CD3-APC (BioLegend, 317318), CD56-BV711 (BioLegend, 362541), CD62L-BV605 (BioLegend, 304833), CD44-BV785 (Biolegend, 103041), EpCAM-PE (BioLegend, 324206), HTII-280 (Terrace Biotech, 303118), and CD66c-BUV395 (BD, 742689). After 30 min incubation, goat anti-mouse IgM Alexa Fluor 488 (Thermo Fisher; A-21042) was added to label HTII-280+ cells. DAPI (0.2 μg/ml), DRAQ7 (CST, 1:1000), and Zombie NIR (BioLegend,

Author Manuscript

Author Manuscript

Author Manuscript

Author Manuscript

423105) were used to exclude dead cells. Cells were sorted into FACS buffer. FACS analysis was performed by FACSDiva (BD).

Histology and Immunohistochemistry—For paraffin embedded mouse lungs, mouse right ventricles were perfused with 1 ml PBS and the lungs were inflated with 4% PFA, and then fixed in 4% PFA overnight at 4°C. After fixation, the lungs were washed by cold PBS X 4 times in 2 hrs at 4°C and dehydrated in a series of increasing ethanol concentration washes (30%, 50%, 70%, 95% and 100%). The dehydrated lungs were incubated with Xylene for 1 hr at RT and with paraffin at 65°C for 90 min X 2 times, and then embed in paraffin and sectioned. For frozen OCT- embedding, lungs were inflated and fixed with 4% PFA for 1 hour at 4°C, washed with PBS for 4 hrs at 4°C, and embedded in OCT after 30% sucrose incubation. Antibodies used were GFP (1:250, Aves Labs, GFP-1020), RFP (1:250, RockLand, 600-401-379), and CD3 (1:200, Abcam, ab16669). Human lung fragments were fixed and processed as the mouse lungs. Antibodies used for human lung slide staining were CD3 (1:100, Origene, UM500048), CD69 (1:100, R&D, AF2359), and CD66c (1:100, Biolegend, 908601). SFTPC (1:250, Millipore, ab3786) and CD44 (1:200, BioLegend, 103001) were used in both mouse and human lung staining.

The Elastin staining was performed according to according to the manufacturer's instructions (Abcam, ab150667). Briefly, the deparaffinized slides were immersed in elastin stain solution for 18 mins and sodium thiosulfate for 1 min. After rinsing, the slides were then stained with Van Gieson's solution for 1 min. Images were captured using Zeiss Imager M1 and analyzed using Axiovision 4.8.2 (Zeiss, Germany) and Fiji software.

3D Tissue Preparation and Imaging—For detection of vascular-associated lymphocyte, mice were injected with 3 μg of AF647-conjugated CD45 antibody by tail vein injection 5 mins prior to euthanasia. Right after, mice were trasncardially perfused with pre-warmed 1X DPBS with 0.2% heparin followed by 4% PFA. Lungs were harvested and post-fixed in fresh 4% PFA overnight at 4°C. After wash with 1X DPBS, coronal sections of 200 μm were prepared using a vibratome (Precisionary Compresstome VF-310-0Z). Samples were washed and incubated in permeabilization buffer (DPBS/0.1%Triton X-100/0.3M glycine) for 1 day at RT, then blocked in DPBS/0.1% TritonX-100/5% serum (from the same host species as the secondary antibody) at 4°C overnight. After, samples were washed in DPBS/0.1% Triton X-100 once and incubated with primary antibodies diluted in DPBS/0.1% Triton X-100/3% serum at RT until the next day. Next, samples were washed in DPBS/0.1% Triton X-100 for 30 min, 3–4 times, then incubated with secondary antibodies diluted in DPBS/0.1% Triton X-100/3% serum at RT for 8 h/overnight. Samples were washed in DPBS/0.1% Triton X-100 or 1 day and finally keep them in 1X DPBS. Before imaging, samples were soaked in RIMS (Refractive Index Matching Solution: 80% Histodenz in 1X PBS, 0.01% sodium azide, 0.1% Tween20) until transparent, then mounted in fresh RIMS solution and scanned. For identification and localization of TRLs to anatomical structures, lung tissues were stained with anti-CD3 (1:100) and anti-aSMA (1:200). All preparations were scanned using a Nikon A1R laser scanning confocal including 405, 488, 561, and 650 laser lines for excitation and imaging with 16X/0.8 or 25X1.1, NA Plan Apo long working distance water immersion objectives. Z steps were acquired every 3 μm.

Author Manuscript

RNAscope and PLISH—Mouse *Il7* probe for RNA in situ detection was purchased from Advanced Cell Diagnotics. OCT- embedded Gli1-labelled lung sections were used for *Il7* RNA in situ detection using the RNAscope Multiplex Fluorescent Reagent Kit v2 (Advanced Cell Diagnotics) according to the manufacturer's instructions. Proximity ligation in situ hybridization (PLISH) was used for detecting the expression of *Hhip* in OCT-embedded Gli1-labelled lungs as previously described [16]. After RNA detection, the slides were further stained with RFP and GFP antibodies.

Cell Culture and Lung Organoids—Primary mouse lung fibroblasts were cultured in DMEM/F-12 (Thermo Fisher) with 10% FBS and 1% PS. The medium was changed every 3 days and lung fibroblasts were maintained for no more than five passages. For SHH stimulation, the confluent fibroblasts were cultured in 0.5 % FBS with 1% PS, and recombinant SHH (R&D) was added at 50 ng/ml with/without 2.5 μg/ml recombinant HHIP (R&D). Then RNA was extracted from the cells after 3 days. For generating the conditioned media for mouse TRL culture, the confluent fibroblasts were treated similar as above, but cultured in advanced RPMI 1640 medium (Thermo Fisher) with 0.5 % FBS, 1% PS, and 2 mM L-Glutamine (Thermo Fisher). After 4 days, the conditioned media were collected and supplemented with 10 % FBS, 100 U/ml IL2 (NCI), 20 ng/ml IL12 (R&D), 10 ng/ml IL18 (R&D), 50 μM β-mercaptoethanol, 5 μl mouse T-Activator CD3/CD28 beads (Thermo Fisher). Then 15,000 TRLs were added into each well of 96-well U-bottom plate with 200 μl supplemented conditioned medium with 30 μg/ml anti-IL7 (R&D) or isotype IgG (R&D) for 7 days. The medium was changed at day 4. To test the direct effect of SHH on TRLs, the fresh medium was used instead of conditioned medium, and the rest treatments and supplements were the same. The number of TRLs were analyzed by flow cytometry using Counting Beads (Thermo Fisher).

For mouse AT2 only organoid assay, tdT+ AT2s were sorted from Tam-injected $Sftpc^{creERT2/+}:R26R^{tdTomato}$ mouse lungs. Then AT2s were resuspended in a feeder-free medium modified from the previously reported study [47]. Briefly, advanced DMEM/F12 medium was supplemented with 10 μM SB431542, 3 μM CHIR, 1 μM BIRB796, 50 ng/ml mouse EGF, 10 ng/ml mouse FGF10, 10 ng/ml mouse IL-1β, 5 μg/ml Heparin, 1X B-27 supplement, 1X Antibiotic-Antimycotic, 15 mM HEPES, 1X GlutaMAX, 1.25 mM N-Acetyl-L-Cysteine, and 10% FBS. The resuspended AT2s were mixed with an equal volume of Matrigel. 50 μl of the mixture (2-3X 10^3 AT2s) was added in each well of 12-well plate, and 1 ml medium was added to each well after Matrigel solidification. For mouse AT2-TRL coculture, 1X10^4 TRLs were added into the well of 12-well plate with 30 μl mouse T-Activator CD3/CD28 beads (Thermo Fisher), and the medium were supplemented with 100 U/ml human IL2 (NCI), 20 ng/ml mouse IL12 (R&D), and 10 ng/ml mouse IL18 (R&D). Where applicable, 1 ng/ml recombinant mouse IFN-γ (R&D) and 30 μg/ml anti-mouse IFN-γ (BioXCell) or isotype IgG (BioXCell) were added to the media. 10 μM Y-27632 was added in the medium for the initial 3 days. The medium was changed every 3-4 days. The mouse organoids were analyzed at day 6.

For human AT2 only organoid assay, sorted CD66c− and CD66c+ AT2s were cultured in 12-well plate the same as the mouse AT2s, except for the medium. The human AT2 organoid medium were previously reported [36], which contains 10 μM SB431542, 3 μM CHIR, 1

Author Manuscript Author Manuscript Author Manuscript Author Manuscript

μM BIRB796, 50 ng/ml human EGF, 10 ng/ml human FGF10, 5 μg/ml Heparin, 1X B-27 supplement, 1X Antibiotic-Antimycotic, 15 mM HEPES, 1X GlutaMAX, and 1.25 mM N-Acetyl-L-Cysteine. For human AT2-TRL coculture, 5X 10^3 CD66c+ AT2s in 45 μl medium were mixed with an equal volume of Matrigel, seeded in a transwell, and incubated in 600 μl medium in a 24-well plate. 1X10^4 human TRLs were added into the well of 24-well plate with 30 μl human T-Activator CD3/CD28 beads (Thermo Fisher), and the medium were supplemented with 100 U/ml human IL2 (NCI), 20 ng/ml human IL12 (R&D), and 10 ng/ml human IL18 (R&D). Where applicable, 5, 10, and 20 ng/ml recombinant human IFN-γ (R&D) and 20 μg/ml anti-human IFN-γ (BioXCell) or isotype IgG (BioXCell) were added to the medium. 10 μM Y-27632 was added in the medium for the initial 3 days. The medium was changed every 3-4 days. The human organoids were analyzed at day 14.

For T cell survival assay, lung resident T cells from sex-matched wildtype C57BL/6 mice were collected and processed for flow cytometry as listed under “Lung Dissociation and Flow Cytometry”. Mice were administered fluorescently conjugated anti-CD45 via retro-orbital injection 3 minutes prior to sacrifice to label circulating immune cells. Fluorescence-activated cell sorting was used to isolate lung resident T cells (gated as live, ivCD45−CD45+CD11b−CD3+). Isolated T cells from multiple mice were pooled together and then plated at 35,000 per well of a round-bottom 96 well plate in 200ul T cell media (Advanced RPMI 1640, 10%FBS, 2mM L-glutamine, 1mM sodium pyruvate and 50uM beta-mercaptoethanol). Recombinant mouse IL-7 (10ng/mL) or recombinant mouse IL-12 (10 ng/mL) were added as indicated. On day 4 of culture, cells were collected and analyzed by flow cytometry with CountBrite Counting Beads to determine absolute cell number. DAPI was used to exclude dead cells from cell count.

Quantitative RT-PCR (qPCR)—Total RNA was obtained from cells, organoids or whole lungs using PicoPure RNA Isolation Kit (Applied Biosystems, KIT0204) or RNeasy mini kit (QIAGEN, 74106), following the manufacturers’ protocols. cDNA was synthesized from total RNA using the SuperScript Strand Synthesis System (Thermo Fisher, 18080044 & 100000840). Quantitative RT-PCR (qRT-PCR) was performed using the SYBR Green system (Thermo Fisher, F415L). Primers are listed in KEY RESOURCES TABLE. Relative gene expression levels after qRT-PCR were defined using the ΔΔCt method and normalizing to GAPDH.

Single Cell RNA Sequencing—Single cell sequencing was performed on a 10X Chromium instrument (10X Genomics, Pleasanton, CA) at the Institute of Human Genetics (UCSF, San Francisco, CA). Briefly, live human lung cells or mouse ivCD45-negative immune cells were sorted and resuspended in 50 μl PBS with 0.04% BSA at 1,000 cells/μl and loaded onto a single lane into the Chromium™ Controller to produce gel bead-in emulsions (GEMs). GEMs underwent reverse transcription for RNA barcoding and cDNA amplification. The library was prepped with the Chromium Single Cell 3’ Reagent Version 3 kit. The samples were sequenced using the HiSeq2500 (Illumina) in Rapid Run Mode.

Bulk Cell RNA Sequencing—For bulk RNAseq of SHH-treated fibroblasts, total RNA from SHH-treated adventitial fibroblasts (PDGFRα+/LY6A+) was isolated using QIAGEN RNeasy Kit according to the manufacturer’s instructions. RNA quality and quantitation were assessed on a Bioanalyzer. 3’-Tag RNAseq library preparation and sequencing was carried by the DNA Technologies and Expression Analysis Core at the UC Davis Genome Center. Briefly, gene expression profiling was carried out using a 3’ Tag-RNA-Seq protocol. Barcoded sequencing libraries were prepared using the Quant- Seq FWD kit (Lexogen) for multiplexed sequencing according to the recommendations of the manufacturer (Lexogen). The fragment size distribution of the libraries was verified via micro-capillary gel electrophoresis on a Bioanalyzer 2100 (Agilent). The libraries were quantified by fluorometry on a Qubit fluorometer (LifeTechnologies), and sequenced on a HiSeq 4000 sequencer (Illumina).

For the bulk RNAseq of lung fibroblasts of $Ubc^{creERT2/+}$:$Myh11^{creERT2/+}$:$Hhip^{flox/flox}$ and $Hhip^{flox/flox}$ mice. Mice were injected with Tamoxifen and maintained for 1 month. Lung fibroblasts were then isolated by FACS. Total RNA was extracted using the Qiagen RNeasy Kit. Sequencing was performed using HiSeq 4000.

QUANTIFICATION AND STATISTICAL ANALYSIS

Statistical Analysis—Statistical analysis was carried out using GraphPad Prism software. One-tailed Student’s t tests were used to generate P values. One-way analysis of variance (ANOVA) was used to determine whether there were statistical differences among three groups followed by Fisher’s least significant difference (LSD) test for pairwise comparisons if the overall test was statistically significant. A P value less than 0.05 was considered significant.

Cell Counting and Image Analysis—At least three samples per genotype/condition were used, and at least 5 randomly selected sections were chosen for each sample. Cell counts for stained cells were performed in Fiji using the “Cell Counter” plug-in. For all analyses, the performers were blinded to the specimen genotype and condition. Results were averaged between each specimen and SD were calculated per condition. Images of CD3/CD69 (human lungs) and CD3/CD44 (mouse lungs) co-staining were processed in Cellprofiler (Broad Institute). Primary objects were generated using the Identify Primary Objects module for each florescent channel. Size and mean intensity filters were applied to remove debris. Double-positive cells were identified by overlapping primary objects with the Relate Objects module. Double-positive cells were used to generate a mask that was applied to both channels of the original image file. For SPC/CD66c (human lungs) co-staining, a mask was applied only to the CD66 channel to remove SPC−/CD66+ cells.

3D Image Analysis and quantification—3D image analysis was performed as previously described [12,48]. Briefly, z-stacks images were rendered in 3D dimensions and quantitatively analyzed using Bitplane Imaris v9.5 software package (Andor Technology PLC, Belfast, N. Ireland). Individual IVCD45+/CD3+ and IVCD45−/CD3+ lymphocytes were annotated using the Imaris spots function based on the colocalization analysis. 3D reconstructions of alpha smooth muscle actin (aSMA)-labeled structures were performed using Imaris surface function and based on the morphological characteristics of blood vessel types and airways. Three dimensional distances between lymphocytes and SMA+ surfaces were calculated using the Imaris Distance Transform Matlab XTension and volumetric

Author Manuscript Author Manuscript Author Manuscript Author Manuscript

decile calculations were performed using a Matlab-based Imaris XTension. Adventitial lymphocytes were defined as spots localized <80-100mm from SMA+ smooth muscle surface and parenchymal lymphocytes as >80-100mm away from SMA+ surfaces.

Contrast-enhanced µCT imaging of lung airspace—Lung specimens were harvested and fixed in 4% PFA at 4°C for 24 hrs. Specimens were then washed 4 times in PBS for 30 mins each time. Lungs were stained in a 25% Lugol's iodine solution at 4°C for 48 hrs. Specimens were then embedded in a scanning medium of 3% agarose. Following agarose embedding, lung specimens were scanned on a Scanco Medical µCT 50 high-resolution specimen scanner. X-ray energy was set at 45 kVp and 88 µA. Specimens were scanned at a resolution of 10 µm voxel size and using an integration time of 500 ms. Quantitative analyses were performed using the Scanco µCT Evaluation Program. The region of interest was manually delineated slice by slice to include the entire lung volume, which we called TLV. An upper threshold of 160 grayscale units, out of 1,000, was applied to segment airspace and excluded tissue. A Gaussian filter with a σ of 0.8 and a support of 1 was applied to remove background noise, and the airspace volume, which we called LAV, was then quantified and reported as a ratio of LAV/TLV for each specimen.

Mean linear intercept (MLI) analysis—For alveolar morphometric analysis, mouse lungs were processed according to the above protocol for paraffin embedded samples, with the exception of inflation with 4% PFA at a constant pressure of 25 cm H_2O. The paraffin-embedded lung sections were stained by hematoxylin and eosin (H&E) for analyzing alveolar morphology metric. At least 5 randomly selected sections from each genotype were selected for analysis. The mean linear intercept (MLI) was calculated as the linear sum of the lengths of all lines randomly drawn across the images, divided by the number of intersections between alveolar walls. A minimum of 1000 intercepts from 60 lines drawn across the lung in a randomized fashion were obtained for each lung, and the analysis was carried out on Fiji with the "Cell Counter" plug-in. The space of airway and pulmonary vessels was excluded. Statistical analysis was done using the one tailed Student's t-test. Data are presented as means ± SD.

Single Cell RNA Sequencing Analysis—FASTQ files were run through CellRanger v3.0.2 software with default settings for de-multiplexing, aligning reads with STAR software to GRCh38 or mm10, and counting unique molecular identifiers (UMIs). Seurat package v3 in RStudio was used for downstream analysis [49]. Low-quality cells were filtered (expressing fewer than 200 genes, >15% mitochondrial reads and >7,000 unique gene counts). Principal component analysis was performed on log-normalized and scaled data using 2,000 variable genes. The top 20 principal component analyses were used for clustering and visualized using the UMAP algorithm in the Seurat package. The lists of DEGs were identified with a Model-based Analysis of Single-cell Transcriptomics (MAST) test. Pathway and Upstream Regulator analysises of gene lists containing significantly differentially expressed genes were done with Ingenuity Pathway Analysis (Qiagen). For interactome analysis we used the vignette NicheNet package.

Author Manuscript
Author Manuscript
Author Manuscript
Author Manuscript

Bulk Cell RNA Sequencing Analysis—FastQC v0.72 was used to read raw sequence data and set quality checks. FASTQ files were trimmed with Trimmomatic v0.38.1 to remove low quality reads and any adapter. The reads were mapped with HISAT2 v2.1.0 to the mouse genome (mm10/GRCm38). After mapping, all BAM files were used as input for HTSeq-count v0.91 to calculate transcript coverage. DESeq2 (v2.11.40) was used to find differentially expressed transcripts between samples for each sequencing depth. The ggplot was generated using RStudio.

Supplementary Material

Refer to Web version on PubMed Central for supplementary material.

Acknowledgements

We thank Parnassus Flow Cytometry Core for assistance with cell sorting for bulk and single cell RNA analysis (P30DK063720); Eunice Wan and the Institute for Human Genetics Core for processing of single cell RNA samples and high-throughput sequencing. GEO accession number for raw RNA sequencing data is listed in Materials and Methods. This work is supported by NIH grants R01HL142552, R01HL155622, and Tobacco Related Disease Research Program (TRDRP) New Investigator Award to T.P., R01HL142701 to A.M., TRDRP Postdoctoral Award to C.W., and Nina Ireland Program Award to M.M. for human lung collection.

REFERENCES

1. Fan X & Rudensky AY Hallmarks of Tissue-Resident Lymphocytes. Cell 164, 1198–1211, doi:10.1016/j.cell.2016.02.048 (2016). [PubMed: 26967286]
2. Agusti A & Hogg JC Update on the Pathogenesis of Chronic Obstructive Pulmonary Disease. N Engl J Med 381, 1248–1256, doi:10.1056/NEJMra1900475 (2019). [PubMed: 31553836]
3. Blanco I, Diego I, Bueno P, Casas-Maldonado F & Miravitlles M Geographic distribution of COPD prevalence in the world displayed by Geographic Information System maps. Eur Respir J 54, doi:10.1183/13993003.00610-2019 (2019).
4. Dransfield MT et al. Acute Exacerbations and Lung Function Loss in Smokers with and without Chronic Obstructive Pulmonary Disease. Am J Respir Crit Care Med 195, 324–330, doi:10.1164/rccm.201605-1014OC (2017). [PubMed: 27556408]
5. Linden D et al. Respiratory viral infection: a potential "missing link" in the pathogenesis of COPD. Eur Respir Rev 28, doi:10.1183/16000617.0063-2018 (2019).
6. Pillai SG et al. A genome-wide association study in chronic obstructive pulmonary disease (COPD): identification of two major susceptibility loci. PLoS Genet 5, e1000421, doi:10.1371/journal.pgen.1000421 (2009). [PubMed: 19300482]
7. Ragland MF et al. Genetic Advances in Chronic Obstructive Pulmonary Disease. Insights from COPDGene. Am J Respir Crit Care Med 200, 677–690, doi:10.1164/rccm.201808-1455SO (2019). [PubMed: 30908940]
8. Chuang PT & McMahon AP Vertebrate Hedgehog signalling modulated by induction of a Hedgehog-binding protein. Nature 397, 617–621, doi:10.1038/17611 (1999). [PubMed: 10050855]
9. Peng T et al. Hedgehog actively maintains adult lung quiescence and regulates repair and regeneration. Nature 526, 578–582, doi:10.1038/nature14984 (2015). [PubMed: 26436454]
10. Lao T et al. Haploinsufficiency of Hedgehog interacting protein causes increased emphysema induced by cigarette smoke through network rewiring. Genome Med 7, 12, doi:10.1186/s13073-015-0137-3 (2015). [PubMed: 25763110]
11. Schroder K, Hertzog PJ, Ravasi T & Hume DA Interferon-gamma: an overview of signals, mechanisms and functions. J Leukoc Biol 75, 163–189, doi:10.1189/jlb.0603252 (2004). [PubMed: 14525967]

Author Manuscript

Author Manuscript

Author Manuscript

Author Manuscript

12. Dahlgren MW et al. Adventitial Stromal Cells Define Group 2 Innate Lymphoid Cell Tissue Niches. Immunity 50, 707–722 e706, doi:10.1016/j.immuni.2019.02.002 (2019). [PubMed: 30824323]
13. Dahlgren MW & Molofsky AB Adventitial Cuffs: Regional Hubs for Tissue Immunity. Trends Immunol 40, 877–887, doi:10.1016/j.it.2019.08.002 (2019). [PubMed: 31522963]
14. Cassandras M et al. Gli1(+) mesenchymal stromal cells form a pathological niche to promote airway progenitor metaplasia in the fibrotic lung. Nat Cell Biol 22, 1295–1306, doi:10.1038/s41556-020-00591-9 (2020). [PubMed: 33046884]
15. Kramann R et al. Perivascular Gli1+ progenitors are key contributors to injury-induced organ fibrosis. Cell Stem Cell 16, 51–66, doi:10.1016/j.stem.2014.11.004 (2015). [PubMed: 25465115]
16. Tsukui T et al. Collagen-producing lung cell atlas identifies multiple subsets with distinct localization and relevance to fibrosis. Nat Commun 11, 1920, doi:10.1038/s41467-020-15647-5 (2020). [PubMed: 32317643]
17. Buechler MB et al. Cross-tissue organization of the fibroblast lineage. Nature 593, 575–579, doi:10.1038/s41586-021-03549-5 (2021). [PubMed: 33981032]
18. Wang C et al. Expansion of hedgehog disrupts mesenchymal identity and induces emphysema phenotype. J Clin Invest 128, 4343–4358, doi:10.1172/JCI99435 (2018). [PubMed: 29999500]
19. Ramilowski JA et al. A draft network of ligand-receptor-mediated multicellular signalling in human. Nat Commun 6, 7866, doi:10.1038/ncomms8866 (2015). [PubMed: 26198319]
20. Onder L et al. IL-7-producing stromal cells are critical for lymph node remodeling. Blood 120, 4675–4683, doi:10.1182/blood-2012-03-416859 (2012). [PubMed: 22955921]
21. Iolyeva M et al. Interleukin-7 is produced by afferent lymphatic vessels and supports lymphatic drainage. Blood 122, 2271–2281, doi:10.1182/blood-2013-01-478073 (2013). [PubMed: 23963040]
22. Amezcua Vesely MC et al. Effector TH17 Cells Give Rise to Long-Lived TRM Cells that Are Essential for an Immediate Response against Bacterial Infection. Cell 178, 1176–1188 e1115, doi:10.1016/j.cell.2019.07.032 (2019). [PubMed: 31442406]
23. Hogg JC et al. The nature of small-airway obstruction in chronic obstructive pulmonary disease. N Engl J Med 350, 2645–2653, doi:10.1056/NEJMoa032158 (2004). [PubMed: 15215480]
24. Browaeys R, Saelens W & Saeys Y NicheNet: modeling intercellular communication by linking ligands to target genes. Nat Methods 17, 159–162, doi:10.1038/s41592-019-0667-5 (2020). [PubMed: 31819264]
25. Henry CJ, Ornelles DA, Mitchell LM, Brzoza-Lewis KL & Hiltbold EM IL-12 produced by dendritic cells augments CD8+ T cell activation through the production of the chemokines CCL1 and CCL17. J Immunol 181, 8576–8584, doi:10.4049/jimmunol.181.12.8576 (2008). [PubMed: 19050277]
26. Barkauskas CE et al. Type 2 alveolar cells are stem cells in adult lung. J Clin Invest 123, 3025–3036, doi:10.1172/JCI68782 (2013). [PubMed: 23921127]
27. Reinhardt RL et al. A novel model for IFN-gamma-mediated autoinflammatory syndromes. J Immunol 194, 2358–2368, doi:10.4049/jimmunol.1401992 (2015). [PubMed: 25637019]
28. Choi J et al. Inflammatory Signals Induce AT2 Cell-Derived Damage-Associated Transient Progenitors that Mediate Alveolar Regeneration. Cell Stem Cell 27, 366–382 e367, doi:10.1016/j.stem.2020.06.020 (2020). [PubMed: 32750316]
29. Jiang P et al. Ineffectual Type 2-to-Type 1 Alveolar Epithelial Cell Differentiation in Idiopathic Pulmonary Fibrosis: Persistence of the KRT8(hi) Transitional State. Am J Respir Crit Care Med 201, 1443–1447, doi:10.1164/rccm.201909-1726LE (2020). [PubMed: 32073903]
30. Kobayashi Y et al. Persistence of a regeneration-associated, transitional alveolar epithelial cell state in pulmonary fibrosis. Nat Cell Biol 22, 934–946, doi:10.1038/s41556-020-0542-8 (2020). [PubMed: 32661339]
31. Belarif L et al. IL-7 receptor blockade blunts antigen-specific memory T cell responses and chronic inflammation in primates. Nat Commun 9, 4483, doi:10.1038/s41467-018-06804-y (2018). [PubMed: 30367166]

Author Manuscript Author Manuscript Author Manuscript Author Manuscript

32. Belarif L et al. IL-7 receptor influences anti-TNF responsiveness and T cell gut homing in inflammatory bowel disease. J Clin Invest 129, 1910–1925, doi:10.1172/JCI121668 (2019). [PubMed: 30939120]
33. Travaglini KJ et al. A molecular cell atlas of the human lung from single-cell RNA sequencing. Nature 587, 619–625, doi:10.1038/s41586-020-2922-4 (2020). [PubMed: 33208946]
34. Kadur Lakshminarasimha Murthy P et al. Human distal lung maps and lineage hierarchies reveal a bipotent progenitor. Nature 604, 111–119, doi:10.1038/s41586-022-04541-3 (2022). [PubMed: 35355018]
35. Basil MC et al. Human distal airways contain a multipotent secretory cell that can regenerate alveoli. Nature 604, 120–126, doi:10.1038/s41586-022-04552-0 (2022). [PubMed: 35355013]
36. Katsura H et al. Human Lung Stem Cell-Based Alveolospheres Provide Insights into SARS-CoV-2-Mediated Interferon Responses and Pneumocyte Dysfunction. Cell Stem Cell 27, 890–904 e898, doi:10.1016/j.stem.2020.10.005 (2020). [PubMed: 33128895]
37. Zacharias WJ et al. Regeneration of the lung alveolus by an evolutionarily conserved epithelial progenitor. Nature 555, 251–255, doi:10.1038/nature25786 (2018). [PubMed: 29489752]
38. Nabhan AN, Brownfield DG, Harbury PB, Krasnow MA & Desai TJ Single-cell Wnt signaling niches maintain stemness of alveolar type 2 cells. Science 359, 1118–1123, doi:10.1126/science.aam6603 (2018). [PubMed: 29420258]
39. Snyder ME et al. Human Lung-Resident Macrophages Colocalize with and Provide Costimulation to PD1(hi) Tissue-Resident Memory T Cells. Am J Respir Crit Care Med 203, 1230–1244, doi:10.1164/rccm.202006-2403OC (2021). [PubMed: 33306940]
40. Sbierski-Kind J, Mroz N & Molofsky AB Perivascular stromal cells: Directors of tissue immune niches. Immunol Rev 302, 10–31, doi:10.1111/imr.12984 (2021). [PubMed: 34075598]
41. Fehrenbach H Alveolar epithelial type II cell: defender of the alveolus revisited. Respir Res 2, 33–46, doi:10.1186/rr36 (2001). [PubMed: 11686863]
42. Negishi H, Taniguchi T & Yanai H The Interferon (IFN) Class of Cytokines and the IFN Regulatory Factor (IRF) Transcription Factor Family. Cold Spring Harb Perspect Biol 10, doi:10.1101/cshperspect.a028423 (2018).
43. Saetta M et al. CD8+ T-lymphocytes in peripheral airways of smokers with chronic obstructive pulmonary disease. Am J Respir Crit Care Med 157, 822–826, doi:10.1164/ajrccm.157.3.9709027 (1998). [PubMed: 9517597]
44. Wang Z et al. Interferon gamma induction of pulmonary emphysema in the adult murine lung. J Exp Med 192, 1587–1600, doi:10.1084/jem.192.11.1587 (2000). [PubMed: 11104801]
45. Kaur M et al. T lymphocyte insensitivity to corticosteroids in chronic obstructive pulmonary disease. Respir Res 13, 20, doi:10.1186/1465-9921-13-20 (2012). [PubMed: 22417244]
46. Chapman HA et al. Integrin alpha6beta4 identifies an adult distal lung epithelial population with regenerative potential in mice. J Clin Invest 121, 2855–2862, doi:10.1172/JCI57673 (2011). [PubMed: 21701069]
47. Weiner AI et al. Mesenchyme-free expansion and transplantation of adult alveolar progenitor cells: steps toward cell-based regenerative therapies. NPJ Regen Med 4, 17, doi:10.1038/s41536-019-0080-9 (2019). [PubMed: 31452939]
48. Cautivo KM et al. Interferon gamma constrains type 2 lymphocyte niche boundaries during mixed inflammation. Immunity 55, 254–271 e257, doi:10.1016/j.immuni.2021.12.014 (2022). [PubMed: 35139352]
49. Butler A, Hoffman P, Smibert P, Papalexi E & Satija R Integrating single-cell transcriptomic data across different conditions, technologies, and species. Nat Biotechnol 36, 411–420, doi:10.1038/nbt.4096 (2018). [PubMed: 29608179]

Author Manuscript

Author Manuscript

Author Manuscript

Author Manuscript

Highlights

-Single cell survey of human emphysema reveals the expansion of tissue-resident lymphocytes (TRL)

-Gli1+ fibroblasts in the adventitia provide a niche for TRL through a hedgehog-IL-7 axis modified by *HHIP*, an emphysema variant gene

-Expanded TRLs suppress alveolar stem cell renewal through IFNγ to drive emphysematous changes

-A highly proliferative but interferon-sensitive alveolar stem cell subset is lost in emphysema patients

Author Manuscript Author Manuscript Author Manuscript Author Manuscript

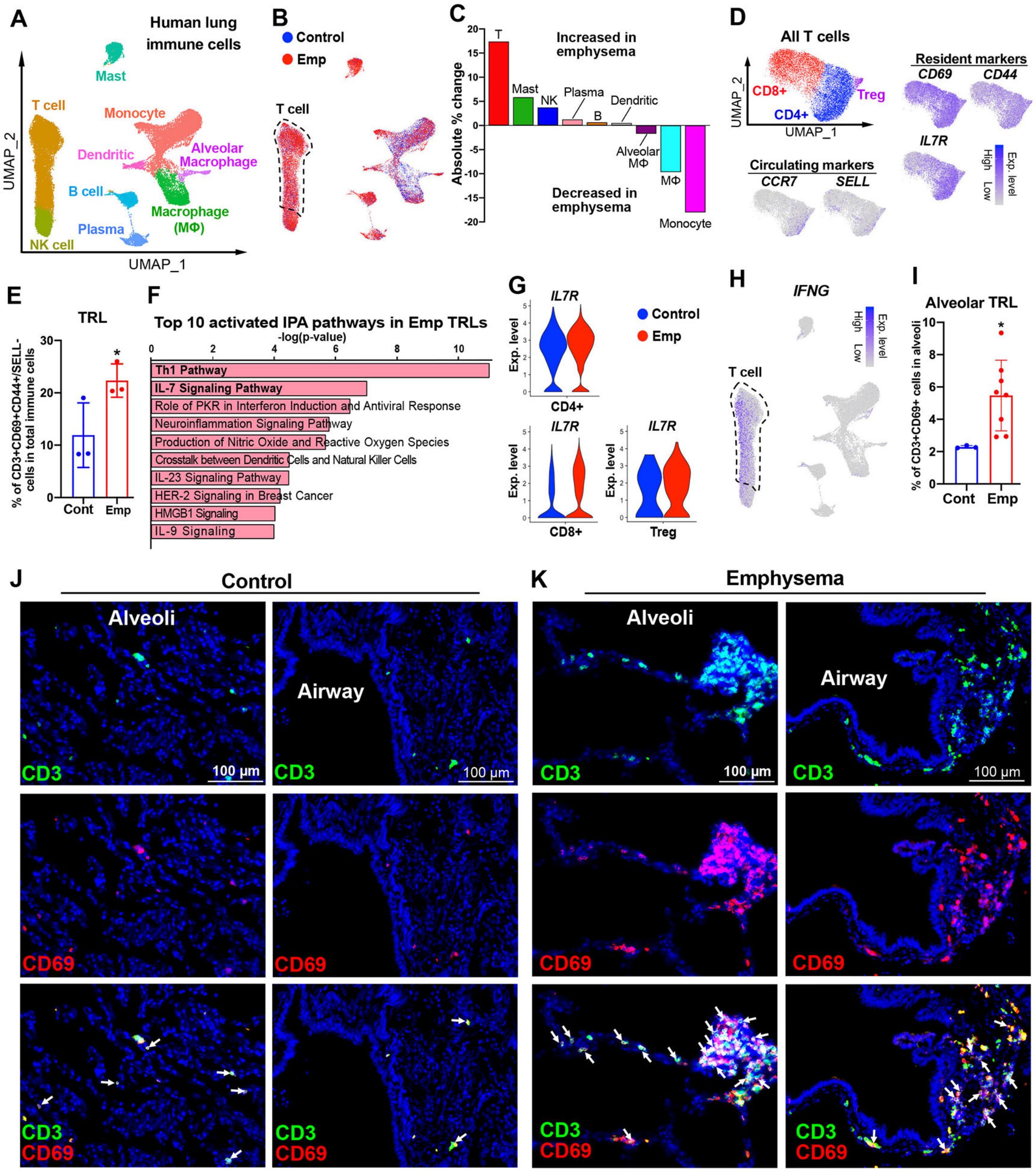

Figure 1. Expansion of tissue-resident lymphocytes in human emphysema lungs.

(A and B) ScRNAseq of $CD45^+$ immune cells from the lung explants of patients undergoing transplantation for COPD/emphysema (Emp, N = 3, Avg. age = 67 ± 5.2 yrs) and cadaveric donors without prior history of lung disease (Control, N = 3, Avg age = 61.3 ± 1.5 yrs).

(C) Absolute change in percentage (% emphysema - % control) of the annotated immune subsets between emphysema and control lungs.

(D) Plots showing the expression of resident markers (*CD69, CD44*, and *IL7R*) and circulating resident markers (*CCR7* and *SELL*) in all T cells.

(E) Percentage of TRLs ($CD3^+/CD69^+/CD44^+/SELL^-$) in total immune cells in emphysema vs. control lungs analyzed from scRNAseq.

(F) Top 10 activated pathways in Emp TRLs, relative to Control TRLs, analyzed with IPA.

Author Manuscript Author Manuscript Author Manuscript Author Manuscript

(G) Violin plots showing *IL7R* expression in CD4$^+$, CD8$^+$, and Treg TRLs (Emphysema vs. Control).

(H) Feature plot showing enriched *IFNG* expression in T cells.

(I) Image quantification of double-positive (CD3$^+$CD69$^+$) T cells as a percentage of all DAPI$^+$ cells in the alveoli of Emp (N = 8) vs. Control (N = 3).

(J and K) Double-positive (CD3$^+$CD69$^+$) T cells in the airway and alveoli of Emp (K) and Control (J). Arrow: CD3$^+$CD69$^+$ T cells.

Mean ± SD, each data point represents one donor. *$p < 0.05$. Emp = emphysema, Cont = Control, TRL = tissue-resident lymphocyte, UMAP = uniform manifold approximation and projection. See also Figure S1 and Supplementary Table 1 and 2

Author Manuscript
Author Manuscript
Author Manuscript
Author Manuscript

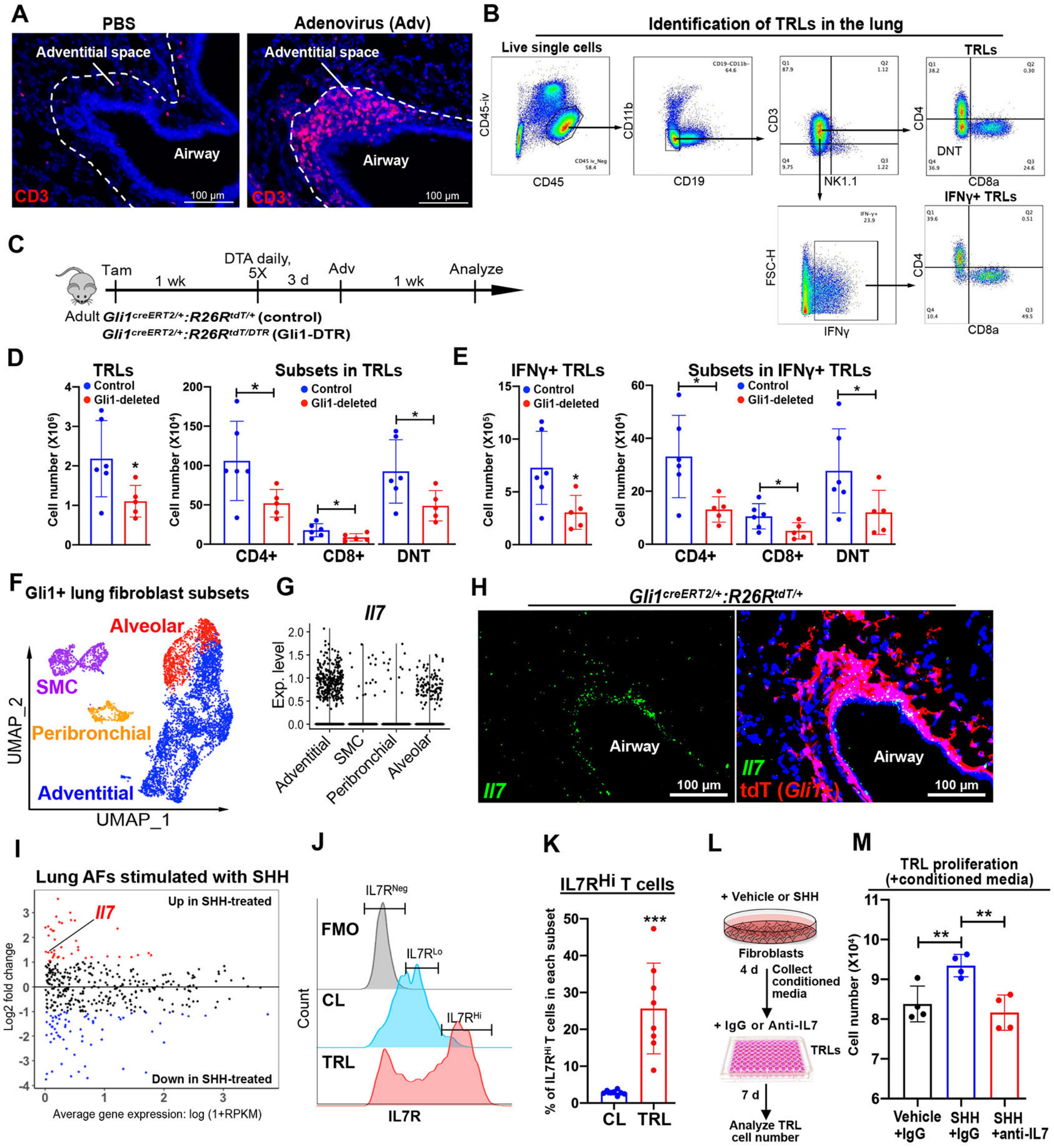

Figure 2. Gli1$^+$ adventitial fibroblast provides a niche for TRLs through hedgehog induction of IL-7.

(A) CD3$^+$ T cells in the adventitial space 7 days after adenoviral (Adv) infection.

(B) FACS strategy to isolate and quantify TRLs in the lung.

(C) Schematics of Gli1$^+$ cell deletion and Adv infection experiment.

(D and E) Quantification of the number of TRLs (**D**) and IFNγ^+ TRL (**E**) subsets in Adv-infected and Gli1-deleted lungs vs. controls by flow cytometry.

(F) scRNAseq analysis of Gli1$^+$ lung fibroblasts showing 4 cell clusters.

(G) Violin plot showing *Il7* expression in the 4 cell clusters of Gli1$^+$ lung fibroblasts.

(H) *Il7* expression (RNAscope *in situ*) and Gli1-labeled cells (tdT+) in the mouse lung.

(I) Altered ligands in SHH-treated lung adventitial fibroblasts, analyzed by bulk cell RNAseq with technical duplicates.

Author Manuscript Author Manuscript Author Manuscript Author Manuscript

(J) Flow histograms of IL7R^{Neg}, IL7R^{Lo}, and IL7R^{Hi} populations in CLs, TRLs, and Fluorescence Minus One (FMO) control.

(K) IL7R^{Hi} cells in TRLs vs. CLs.

(L) Schematics of conditioned media generation and TRL proliferation experiment.

(M) Quantification of number of TRLs after conditioned media culture, with anti-IL7 or IgG isotype.

Mean ± SD, each data point represents one mouse (D, E, and K) or one technical replicate (M) of an individual experiment. All *in vitro* experiments have been repeated at least one time with consistent results for validation. *p < 0.05; **p < 0.005; ***p < 0.0005. Adv = adenovirus, TRL = tissue-resident lymphocyte, AF = adventitial fibroblast, CL = circulating lymphocyte. See also Figure S2 and S3, and Supplemental Table 3.

Author Manuscript

Author Manuscript

Author Manuscript

Author Manuscript

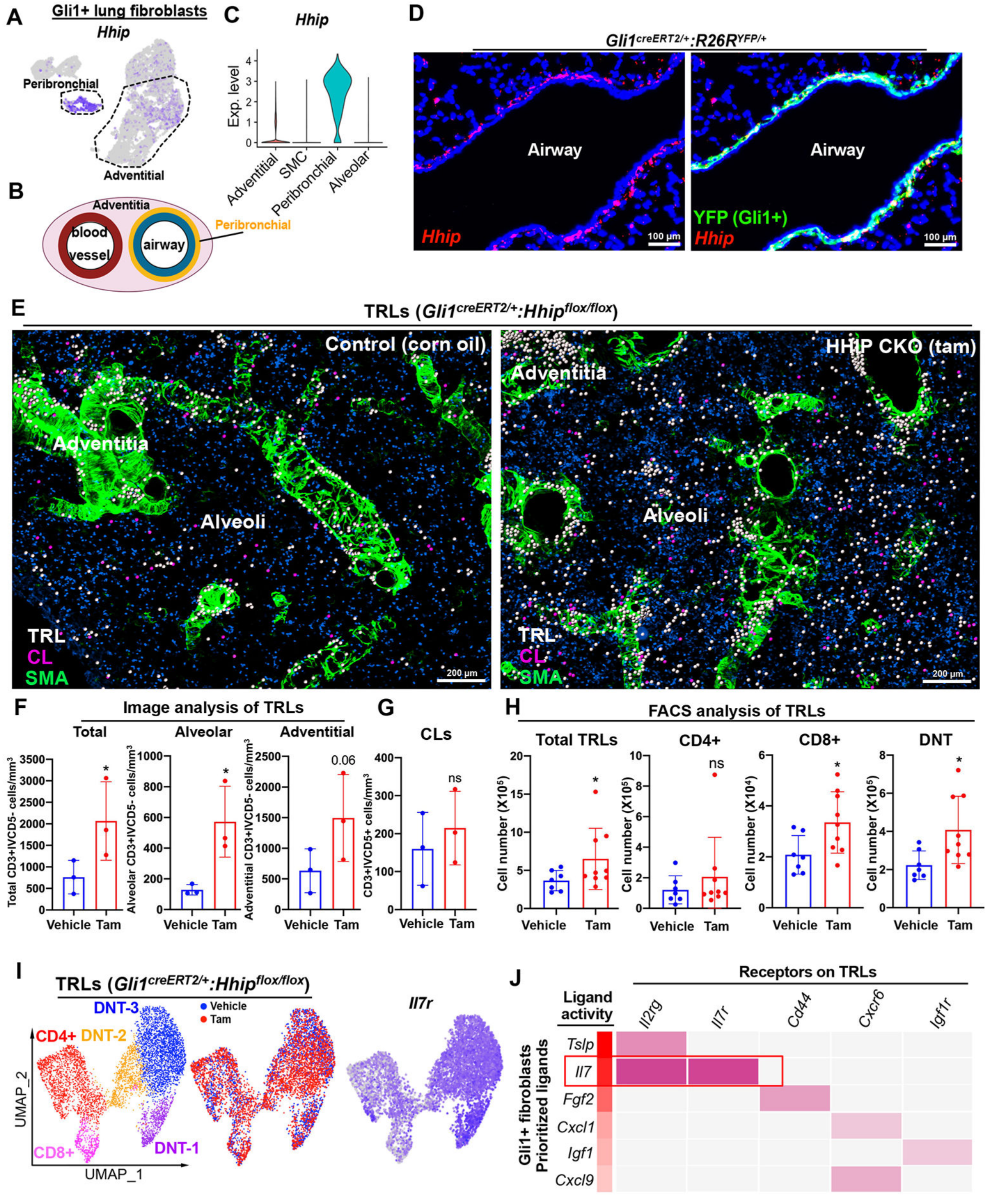

Figure 3. Stromal-specific loss of HHIP induces TRL expansion

(A) Feature plot showing *Hhip* expression in Gli1^{+} fibroblasts.

(B) Fibroblast localization in the adventitia.

(C) *Hhip* expression in Gli1+ lung fibroblasts subsets.

(D) *Hhip* expression (PLISH) and Gli1-labelled cells (YFP+) in the mouse lung.

(E) Thick-section confocal imaging of lungs 6 months after adventitial-specific deletion of *Hhip* with tamoxifen induction.

(F and G) Image quantification of TRLs and CLs in the lungs of Tam or vehicle-injected *Gli1$^{creERT2/+:}$Hhip$^{flox/flox}$* mice.

(H) Flow quantification of TRLs (total, CD4^{+}, CD8^{+}, and DNT) in the lungs of Tam or vehicle-injected *Gli1$^{creERT2/+:}$Hhip$^{flox/flox}$* mice.

Author Manuscript Author Manuscript Author Manuscript Author Manuscript

(I) scRNAseq analysis of TRLs from the lungs of Tam or vehicle-injected $Gli1^{creERT2/+:}Hhip^{flox/flox}$ mice.

(J) NicheNet interactome analysis of scRNAseq datasets of TRLs (DEG of TRLs from $Gli1^{HHIPCKO}$ vs control lungs) and $Gli1^{+}$ fibroblasts.

Mean ± SD, each data point represents one mouse (F-H) of an individual experiment. ns, $p > 0.05$; $^{*}p < 0.05$. TRL = tissue-resident lymphocyte, CL = circulating lymphocyte. See also Figure S4 and S5.

Author Manuscript

Author Manuscript

Author Manuscript

Author Manuscript

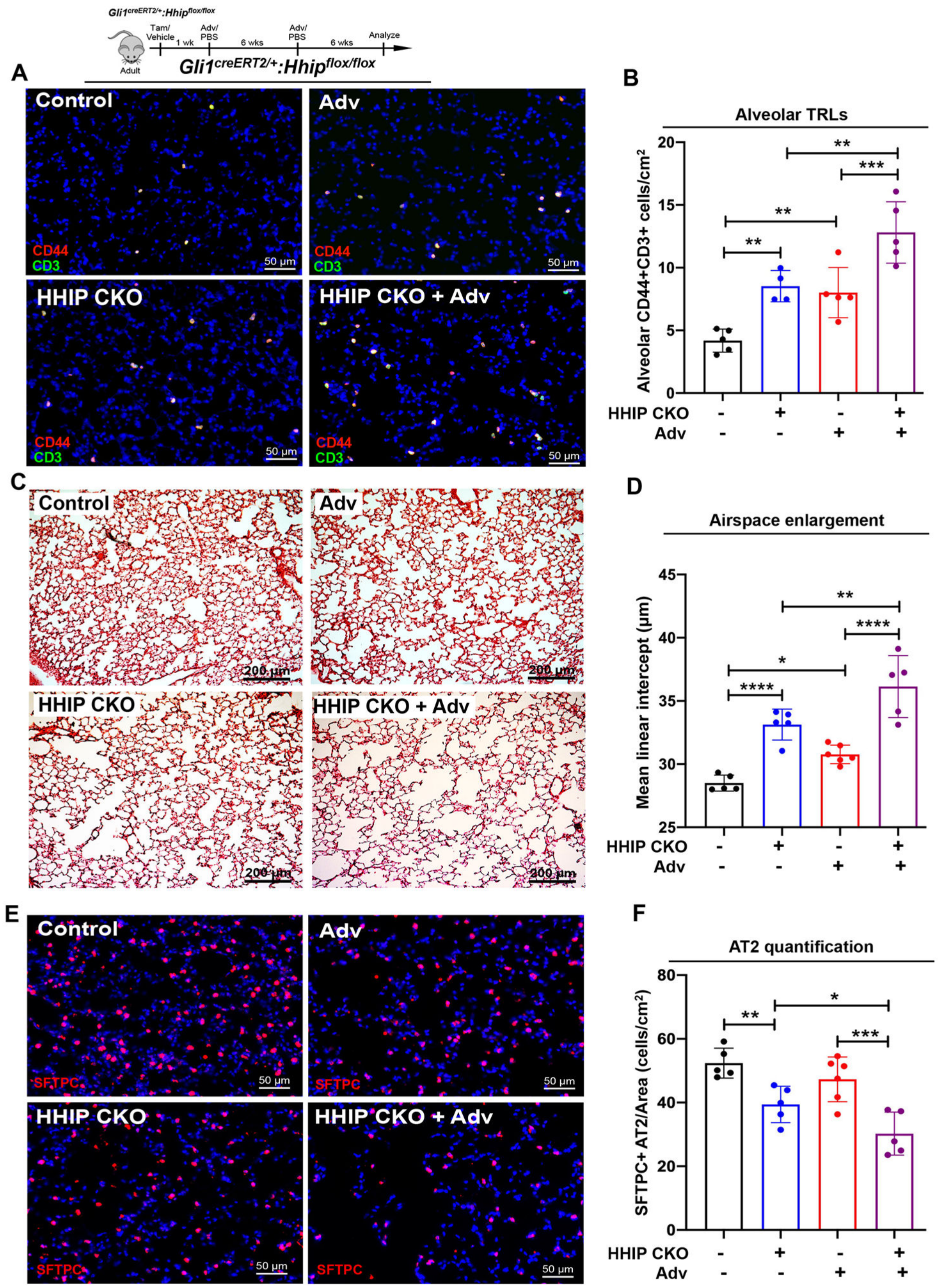

Figure 4. Stromal-specific HHIP deletion potentiates loss of alveoli accompanying viral infections.

(A and B) TRLs (CD3$^+$/CD44$^+$) in the lungs of vehicle or Tam-injected *Gli1$^{creERT2/+}$:Hhip$^{flox/flox}$* mice treated with adenoviruses or PBS.

(C and D) H&E images (C) and mean linear intercept analysis (D) of the lungs from vehicle or Tam-injected *Gli1$^{creERT2/+}$:Hhip$^{flox/flox}$* mice treated with adenoviruses or PBS.

(E and F) AT2 (SFTPC+) in the lungs from vehicle or Tam-injected *Gli1$^{creERT2/+}$:Hhip$^{flox/flox}$* mice treated with adenoviruses or PBS.

Author Manuscript Author Manuscript Author Manuscript Author Manuscript

Mean ± SD, each data point represents one mouse (B, D, and F). *$p < 0.05$; **$p < 0.005$; ***$p < 0.0005$; ****$p < 0.0001$. Adv = adenovirus, Tam = tamoxifen, AT2 = alveolar type 2 cell. See also Figure S6.

Author Manuscript
Author Manuscript
Author Manuscript
Author Manuscript

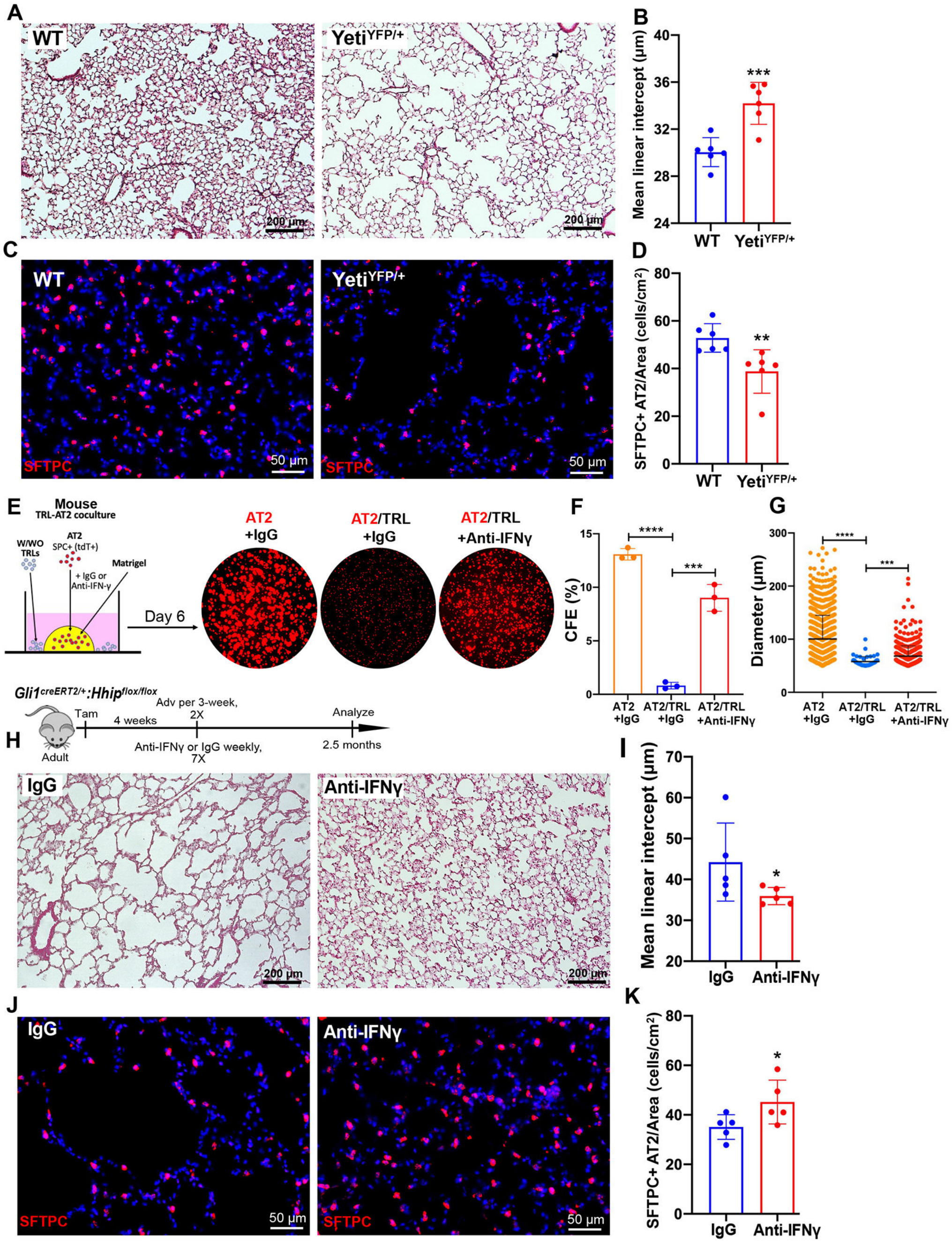

Figure 5. IFNγ drives emphysematous changes after viral exacerbation

(A and B) Images and mean linear intercept of the wild-type (WT) and Yeti$^{YFP/+}$ lungs.

(C and D) SFTPC$^+$ AT2s (D) in the lungs of WT and Yeti$^{YFP/+}$ mice (3-month-old).

(E) Schematics of mouse AT2 (tdT$^+$) and TRL co-culture experiment.

(F and G) Colony-forming efficiency (F) and size (G) analyses of organoids cultured with or without TRLs and treated with anti-IFNγ or IgG isotype.

(H and I) H&E images and MLI of *Gli1*$^{creERT2/+}$:*Hhip*$^{flox/flox}$ mice followed by adenoviral infections treated with anti-IFNγ or IgG isotype. IgG isotype or anti-IFNγ.

Author Manuscript Author Manuscript Author Manuscript Author Manuscript

(J and K) AT2s (SFTPC$^+$) in the virus-infected *Gli1*$^{creERT2/+}$:*Hhip*$^{flox/flox}$ mice treated with anti-IFNγ or IgG isotype.

Mean ± SD, each data point represents one mouse (B, D, I and K), one technical replicate (F), and one organoid (G) of an individual experiment. All *in vitro* experiments have been repeated at least one time with consistent results for validation. *p < 0.05; **p < 0.005; ***p < 0.0005; ****p < 0.0001. Adv = adenovirus, Tam = tamoxifen, AT2 = alveolar type 2 cell, CFE = colony forming efficiency. See also Figure S6.

Author Manuscript

Author Manuscript

Author Manuscript

Author Manuscript

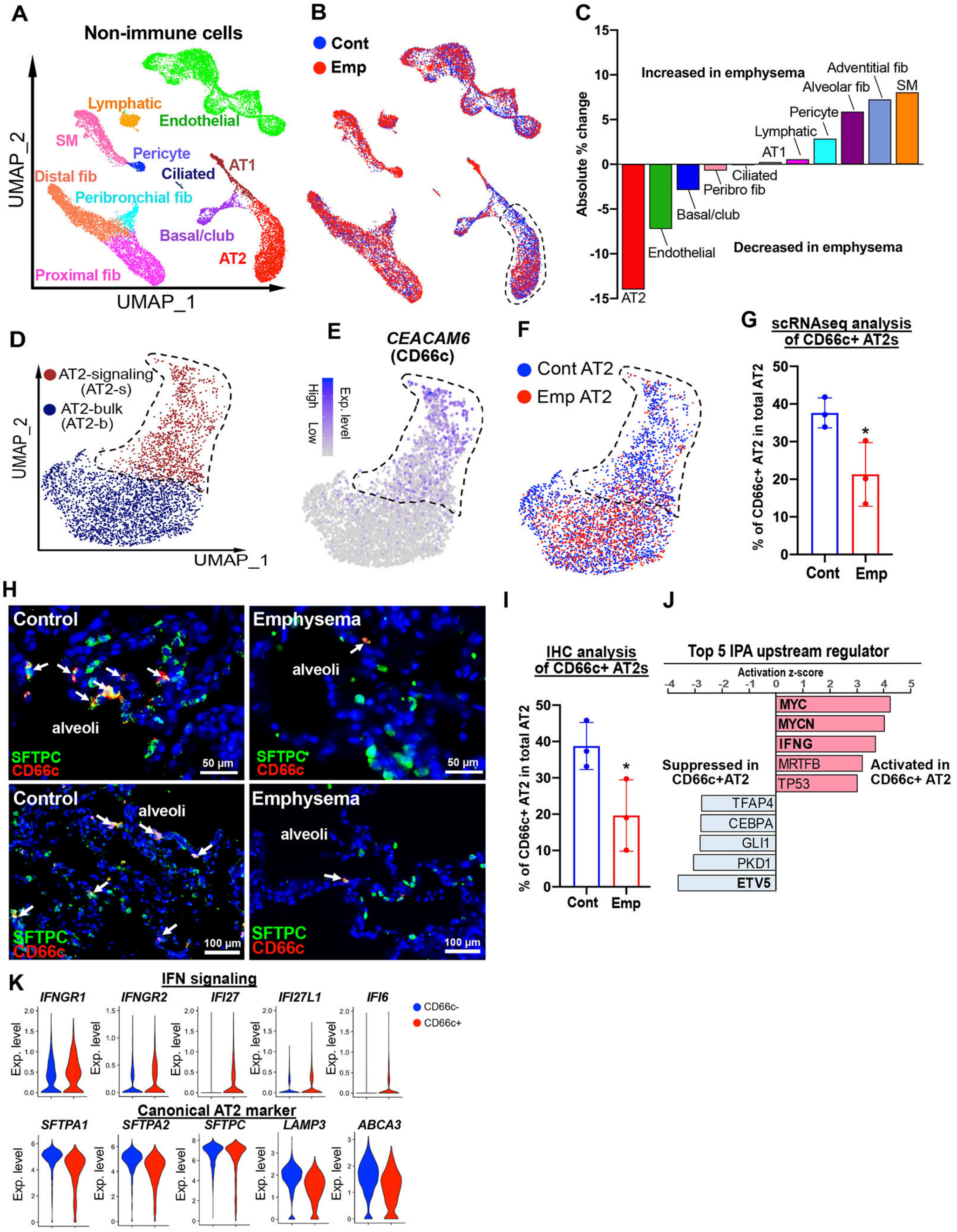

Figure 6. Loss of an IFN-poised AT2 subset in COPD/emphysema lungs

(A and B) ScRNAseq of non-immune cells from the lung explants of patients undergoing transplantation for COPD/emphysema (Emp, N = 3) and age matched cadaveric donors without prior history of lung disease (Control, N = 3).

(C) Absolute change in percentage (% emphysema - % control) of the annotated non-immune subsets between emphysema and control lungs.

(D-F) Segregation of two distinct AT2 clusters on UMAP in the human lung **based on** *CEACAM6* (CD66c) expression and loss of CD66c$^+$ AT2s in emphysema lungs.

Author Manuscript

Author Manuscript

Author Manuscript

Author Manuscript

(G) Quantification of CD66c+ AT2s as a percentage of total AT2s in Emp vs. Control lungs on scRNAseq.

(H and I) CD66c$^+$ AT2s as a percentage of total AT2s (SFTPC$^+$) in Emp vs. Cont.

(J) Top 5 activated and suppressed upstream regulators in CD66c$^+$ vs. CD66c$^-$ AT2s.

(K) Expression of IFNγ signaling genes and AT2 markers in CD66c$^+$ vs. CD66c$^-$ AT2s.

Mean ± SD, each data point represents one donor (G and I). $^*p < 0.05$. Emp = emphysema, AT2 = alveolar type 2 cells, UMAP = uniform manifold approximation and projection. See also Figure S7.

Author Manuscript

Author Manuscript

Author Manuscript

Author Manuscript

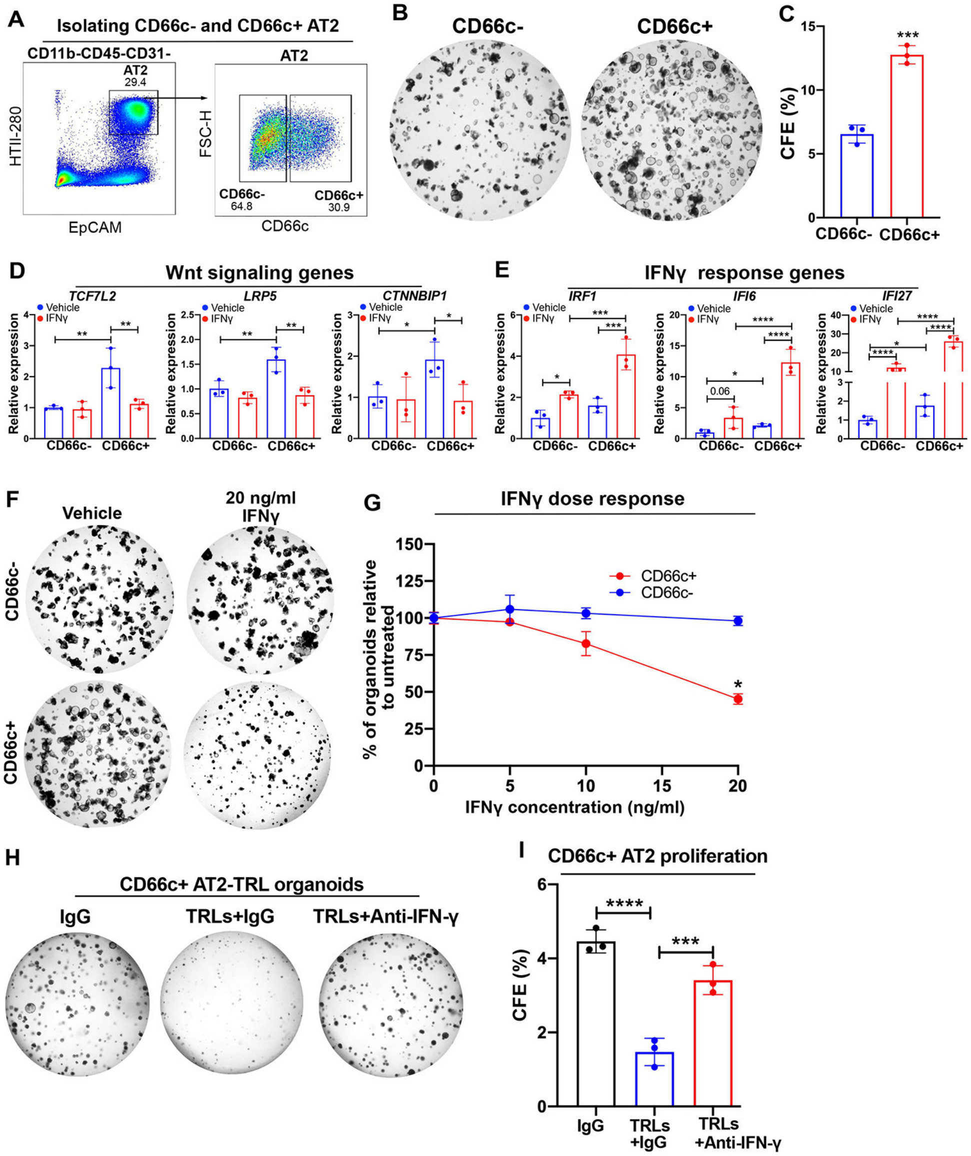

Figure 7. Human lung TRLs directly suppress CD66c$^+$ AT2s *via* IFNγ

(A) Flow panel of using CD66c to segregate HTII-280$^+$ AT2s for isolation from the human lung.

(B and C) Images (B) and colony forming efficiency (C) analysis of organoids derived from CD66c$^-$ and CD66c$^+$ AT2s.

(D and E) qPCR analyses of Wnt signaling (D) and IFNγ response (E) genes in CD66c$^-$ and CD66c$^+$ AT2s treated with/without IFNγ.

(F and G) Images (F) and percentage of viable organoids (G, percentage of vehicle treated group) from CD66c$^-$ and CD66c$^+$ AT2s treated with escalating doses of IFNγ.

(H and I) Images (H) and colony forming efficiency (I) of CD66c$^+$ AT2s organoids cultured with/without TRLs and treated with anti-IFNγ or IgG isotype.

Author Manuscript

Author Manuscript

Author Manuscript

Author Manuscript

Mean ± SD, each data point represents one technical replicate of an individual experiment (C-E, G, and I). All *in vitro* experiments have been repeated at least one time with consistent results for validation

Author Manuscript Author Manuscript Author Manuscript Author Manuscript

KEY RESOURCES TABLE

REAGENT or RESOURCE	SOURCE	IDENTIFIER
Antibodies		
Rabbit anti-human/mouse SFTPC (used at 1:2000)	Millipore Sigma	Cat#AB3786; RRID: AB 91588
Goat anti-human SCGB3A2 (used at 1:200)	R&D	Cat#AF3545; RRID: AB 2183543
Chicken anti-GFP (used at 1:250)	Aves Labs	Cat#GFP-1020; RRID: AB 10000240
Rabbit anti-RFP (used at 1:250)	Thermo Fisher	Cat# 600-401-379; RRID: AB 2209751
Rabbit anti-mouse CD3 (used at 1:200)	Abcam,	Cat#ab16669; RRID: AB 443425
Rabbit anti-mouse CD20 (used at 1:200)	Abcam	Cat#ab64088; RRID: AB 1139386
Rat anti-mouse CD8a (used at 1:200)	R&D	Cat# MAB116; RRID: AB 357497
Rat anti-mouse KRT8 (used at 1:200)	DSHB	Cat#TROMA-I; RRID: AB 531826
Rat Anti-human/mouse CD44 (used at 1:200)	BioLegend	Cat#103001; RRID:AB 312952
Goat anti-human CD69 (used at 1:100)	R&D	Cat#AF2359; RRID: AB 355231
Mouse anti-human CD3 (used at 1:100)	OriGene	Cat#UM500048; RRID: AB 2629062
Mouse anti-human CD66c (used at 1:100)	BioLegend	Cat#908601, RRID:AB 2565088
Donkey Anti-chicken IgY (H+L), Alexa Fluor 647 (used at 1:250)	Jackson ImmunoResearch	Cat# 703-605-155; RRID: AB 2340379
Donkey anti-rabbit IgG (H+L), Alexa Fluor 555 (used at 1:250)	Thermo Fisher	Cat# A-31572; RRID: AB 162543
Donkey anti-rabbit IgG (H+L), Alexa Fluor 488 (used at 1:250)	Thermo Fisher	Cat#A-21206; RRID: AB 2535792
Donkey anti-mouse IgG (H+L), Alexa Fluor 647 (used at 1:250)	Thermo Fisher	Cat#A31571; RRID: AB 162542
Donkey anti-goat IgG (H+L), Alexa Fluor 594	Thermo Fisher	Cat#A-11058; RRID: AB 2534105
Donkey Anti-rat IgG (H+L), Alexa Fluor 488 (used at 1:250)	Thermo Fisher	Cat# A-21208; RRID: AB 2535794
Goat anti-mouse IgM Antibody Alexa Fluor 488 (used at 1:250)	Thermo Fisher	Cat# A-21042; RRID: AB 2535711
Rat anti-mouse CD45 Alexa Fluor 700 (used at 1:200)	BD	Cat#560510; RRID: AB 1645208
Rat Anti-mouse CD45 BUV395 (used at 1:200)	BD	Cat#565967; RRID: AB 2739420
Rat Anti-mouse CD45-BV421 (used at 3 µg/mouse IVCD45)	BD	Cat# 563890; RRID: AB 2651151
Rat anti-mouse CD11b BV605 (used at 1:1000)	BD	Cat# 563015; RRID: AB 2737951
Rat anti-mouse CD3e APC (used at 1:200)	BioLegend	Cat# 100312; RRID: AB 312677
Rat anti-mouse CD3e Alexa Fluor 700 (used at 1:200)	BioLegend	Cat# 100216; RRID: AB 493697
Rat anti-mouse CD4 BV711 (used at 1:200)	BioLegend	Cat#100557; RRID: AB_2562607
Rat anti-mouse CD8a PE (used at 1:200)	BioLegend	Cat# 100707; RRID: AB 312746
Rat anti-mouse CD8a FITC (used at 1:200)	BioLegend	Cat# 100705; RRID: AB 312744
Rat anti-mouse CD19 PE/Dazzle 594 (used at 1:200)	BioLegend	Cat# 115554; RRID: AB 2564001
Rat anti-mouse NK1.1 BV650 (used at 1:200)	BioLegend	Cat# 108736; RRID: AB 2563159
Rat anti-mouse/human CD44 BV785 (used at 1:200)	BioLegend	Cat# 103041; RRID: AB 11218802
Rat anti-mouse CD62L PE (used at 1:200)	BioLegend	Cat# 104407; RRID: AB 313094
Rat anti-mouse IL-4 Alexa Fluor 488	BioLegend	Cat# 504111; RRID: AB 493321
Rat anti-mouse IL-13 PE	Thermo Fisher	Cat#12-7133-82; RRID: AB 763559
Rat anti-mouse IL-17A PE-Cy7	BioLegend	Cat# 506921; RRID: AB 2125011
Rat anti-mouse IFN-γ APC (used at 1:100)	BioLegend	Cat# 505810; RRID: AB 315404
Rat anti-mouse IL7R Alexa Fluor 647 (used at 1:200)	BioLegend	Cat# 135020; RRID: AB 1937209
Rat anti-mouse CD31 PerCP-eFluor 710 (used at 1:200)	Thermo Fisher	Cat# 46-0311-80; RRID: AB 1834430
Rat anti-mouse CD326 BV421 (used at 1:200)	BD	Cat#563214; RRID: AB 2738073

Author Manuscript Author Manuscript Author Manuscript Author Manuscript

REAGENT or RESOURCE	**SOURCE**	**IDENTIFIER**
Rat anti-mouse PDGFRα APC (used at 1:200)	Thermo Fisher	Cat# 17-1401-81; RRID: AB 529482
Rat anti-mouse LY6A APC-Cy7 (used at 1:200)	BioLegend	Cat#108126; RRID: AB 10645327
Mouse anti-human CD45 Alexa Fluor488 (used at 1:200)	BioLegend	Cat# 304019; RRID: AB 493033
Mouse anti-human CD45 APC-Cy7 (used at 1:200)	BioLegend	Cat#304014; RRID: AB_314402
Mouse anti-human CD31 APC-Cy7 (used at 1:200)	BioLegend	Cat#303120; RRID: AB 10640734
Mouse anti-human CD11b APC-Cy7 (used at 1:200)	BD	Cat#557754; RRID: AB 396860
Mouse anti-human CD69 BV421 (used at 1:200)	BioLegend	Cat# 310929; RRID: AB 10933255
Mouse anti-human CD3 APC (used at 1:200)	BioLegend	Cat# 317318; RRID: AB 1937212
Mouse anti-human CD56 BV711 (used at 1:200)	BioLegend	Cat# 362541; RRID: AB 2565919
Mouse anti-human EpCAM PE (used at 1:200)	BioLegend	Cat# 324206; RRID: AB 756080
Mouse anti-human CD62L BV605 (used at 1:200)	BioLegend	Cat# 304833; RRID: AB 2562129
Mouse anti-human CD66c BUV395 (used at 1:200)	BD	Cat# 742689; RRID: AB 2740971
Mouse anti-mouse aSMA Alexa Fluor 488 (used at 1:200)	eBioscience	Cat#53-9760-82; RRID: AB 2574461
Mouse IgM anti-human HTII-280 (used at 1:200)	Terrace Biotech	Cat# 303118; RRID: AB 2247932
Rat anti-mouse IFNγ (XMG1.2)	BioXCell	Cat# BE0055; RRID: AB 493637
Rat IgG1 isotype control	BioXCell	Cat# BE0088; RRID: AB 1107775
Rat anti-IL7R (A7R34)	BioXCell	Cat# BE0065; RRID: 1107590
Rat IgG2 isotype control	BioXCell	Cat# BE0089; RRID: 1107769
Mouse anti-human IFNγ (B133.5)	BioXCell	Cat# BE0235; RRID: AB 2687717
Mouse IgG1 isotype control	BioXCell	Cat# BE0083; RRID: AB 1107784
Goat anti-mouse IL-7	R&D	Cat# AB-407-NA; RRID: AB 354353
Goat IgG isotype control	R&D	Cat# AB-108-C; RRID: AB 354267
Virus Strains		
Ad5-CMV-empty	UI vector core lab	Cat# WC-U of Iowa-272
Biological Samples		
Human COPD/emphysema Lung Tissues	UCSF Lung Disease Blood and Tissue Repository	N/A
Normal Human Lung Tissues	Northern California Transplant Donor Network	N/A
Chemicals, Peptides, and Recombinant Proteins		
DMEM/F-12	Thermo Fisher	Cat#11330032
Advanced DMEM/F-12	Thermo Fisher	Cat# 12634010
RPMI 1640 Medium	Thermo Fisher	Cat#11875093
Advanced RPMI 1640 Medium	Thermo Fisher	Cat#12633012
TrypLE Select Enzyme	Thermo Fisher	Cat#12563011
Fetal Bovine Serum, heat inactivated (FBS)	Thermo Fisher	Cat#12676011
Penicillin/Streptomycin (100x)	Thermo Fisher	Cat#MT30002CI
Antibiotic-Antimycotic (100X)	Thermo Fisher	Cat#A5955-100ML
SB431542	Abcam	Cat#Ab120163
BIRB796	Tocris	Cat#598910
Y-27632	SELLECK CHEM	Cat#S1049
N-Acetyl-L-cysteine	Sigma Aldrich	Cat#A9165

Author Manuscript Author Manuscript Author Manuscript Author Manuscript

REAGENT or RESOURCE	SOURCE	IDENTIFIER
Heparin sodium salt	Sigma Aldrich	Cat#H3149-500KU
Glutamax	Gibco	Cat#35050061
B-27 Supplement (50X)	Thermo Fisher	Cat#17504044
MEM Non-Essential Amino Acids Solution (100X)	Gibco	Cat#11140050
L-Glutamine (200 mM)	Thermo Fisher	Cat#25030-149
Sodium Pyruvate (100 mM)	Gibco	Cat#11360070
2-Mercaptoethanol (50 mM)	Gibco	Cat#31350010
Fluorsave	Millipore Sigma	Cat#345789
DAPI (used 1:1000)	Thermo Fisher	Cat#1738176
DRAQ7 (used 1:1000)	CST	Cat#7406S
RBC Lysis Buffer (10x)	Thermo Fisher	Cat#NC9067514
Normal Donkey Serum	Thermo Fisher	Cat#50413275
4% Paraformaldehyde (PFA) in PBS	Santa Cruz	Cat#sc-281692
Xylene	VWR	Cat#89370-088
Paraffin	Thermo Fisher	Cat#8330
OCT	VWR	Cat#25608-930
Diva Decloaker Antigen Retrieval (10x)	Biocare Medical	Cat#DV2004MX
TritonX-100	Sigma Aldrich	Cat#X100
Tween 20	Thermo Fisher	Cat#BP337500
TrueBlack (50x)	Biotium	Cat#23007
Liberase Tm	Roche	Cat#5401127001
Collagenase type I	Thermo Fisher	Cat#17100017
Dispase II	Thermo Fisher	Cat#17105041
DNase I	Sigma Aldrich	Cat#DN25
Matrigel	Thermo Fisher	Cat#CB-40230A
Tamoxifen	Sigma-Aldrich	Cat#T5648
Corn oil	Sigma Aldrich	Cat#C8267
FcR Blocking Reagent	Miltenyi Biotec	Cat#130-092-575
Human FcR Blocking Reagent	BD	Cat#564220
OneComp Beads	Thermo Fisher	Cat#501129031
SuperScript III Reverse Transcriptase	Thermo Fisher	Cat#18080044
Streptavidin Beads (1:50)	STEMCELL Tech	Cat#17663
RnaseOUT Rnase Inhibitor	Thermo Fisher	Cat#100000840
Diphtheria toxin	Sigma Aldrich	Cat# D0564
Trizol	Thermo Fisher	Cat#15596018
Cell Stimulation Cocktail (500X)	Tonbo Biosciences	Cat#TNB-4975-UL100
Brefeldin A Solution (1000X)	eBioscience	Cat#00-4506-51
Human IL2	NCI	N/A
FTY720	Sigma	Cat#SML0700
Mouse IL-7	R&D	Cat#407ML005CF
Mouse IL-12	R&D	Cat#419-ML-010/CF
Mouse IL-18	R&D	Cat#9139IL010CF

Author Manuscript

Author Manuscript

Author Manuscript

Author Manuscript

REAGENT or RESOURCE	**SOURCE**	**IDENTIFIER**
Mouse IL-1β	BioLegend	Cat#579404
Mouse SHH	R&D	Cat#464SH025CF
Mouse HHIP	R&D	Cat#1568HP050CF
Mouse FGF10	Pepro Tech	Cat#450-61
Mouse EGF	Pepro Tech	Cat#315-09
Mouse IFNγ	R&D	Cat#485MI100
Human IFNγ	R&D	Cat#285-IF
Human IL-12	R&D	Cat#219-IL-005/CF
Human IL-18	R&D	Cat#9124-IL-010/CF
Human FGF10	Pepro Tech	Cat#100-26
Human EGF	Gibco	Cat#PHG0313
Critical Commercial Assays		
Dynabeads Mouse T-Activator CD3/CD28	Thermo Fisher	Cat#11456D
Dynabeads Human T-Activator CD3/CD28	Thermo Fisher	Cat#11161D
PicoPure RNA Isolation Kit	Applied Biosystems	Cat#KIT0204
RNeasy Kit	QIAGEN	Cat#74106
Zombie NIR Fixable Viability Kit	BioLegend	Cat#423105
DyNAmo Flash SYBR Green qPCR Kit	Thermo Fisher	Cat#F415L
RNase-Free DNase Set	QIAGEN	Cat#79254
GoTaq genotyping assay	Promega	Cat#M7823
Intracellular Staining Buffer Set	eBioscience	Cat# 00-5523-00
Elastic stain kit	Abcam	Cat#ab150667
CountBright! Absolute Counting Beads	Invitrogen	Cat#C36950
RNAscope Multiplex Fluorescent Reagent Kit v2	Advanced Cell Diagnotics	Cat#323100
RNAscope Probe Mm_*Il7*	Advanced Cell Diagnotics	Cat#439671
Deposited Data		
Single-cell RNA-seq of human normal and emphysema lungs	This paper	GEO: GSE196638
Single-cell RNAseq of the lung resident immune cells from Gli1HhipCKO_Tam and Gli1HhipCKO_Oil mice	This paper	GEO: GSE206721
Bulk RNAseq of HhipCKO (UBCcreER/Myh11creER/Hhipflox/flox) and control (Hhipflox/flox) fibroblasts	This paper	GEO: GSE209734
Experimental Models: Organisms/Strains		
Mouse: *Hhip*$^{flox/flox}$	This paper	N/A
Mouse: *C57BL/6*	Jackson Laboratory	JAX# 000664
Mouse: *Gli1*^{creERT2}	Jackson Laboratory	JAX# 007913
Mouse: *R26R*^{EYFP}	Jackson Laboratory	JAX# 006148
Mouse: *R26R*^{tdT}	Jackson Laboratory	JAX# 007909
Mouse: *R26R*^{DTR}	Jackson Laboratory	JAX# 007900
Mouse: YetiYFP	(R. Lee Reinhardt et al., 2015)	N/A
Mouse: UbccreERT2	Jackson Laboratory	JAX#007001
Mouse: Myh11creERT2	Jackson Laboratory	JAX#019079
Mouse: SftpccreERT2	(Chapman et al., 2011)	N/A

Author Manuscript Author Manuscript Author Manuscript Author Manuscript

REAGENT or RESOURCE	**SOURCE**	**IDENTIFIER**
Oligonucleotides and plasmid		
Ms_*Il7*_Forward	IDT	5’ TTCCTCCACTGATCCTTGTTCT 3’
Ms_*Il7*_Reverse	IDT	5’ AGCAGCTTCCTTTGTATCATCAC 3’
Ms_*Hhip*_Forward	IDT	5’ GAAACGGCTACTACACCCCC 3’
Ms_*Hhip*_Reverse	IDT	5’ TGGCTCACACTTGGCAATTC 3’
Ms_*Gli1*_Forward	IDT	5’ CCCACTCCAATGAGAAGCCAT 3’
Ms_*Gli1*_Reverse	IDT	5’ CGGACCATGCACTGTCTTCA 3’
Ms_*Ifng*_Forward	IDT	5’ ATGAACGCTACACACTGCATC 3’
Ms_*Ifng*_Reverse	IDT	5’ CCATCCTTTTGCCAGTTCCTC 3’
Ms_*Ifit1*_ Forward	IDT	5’ CTGAGATGTCACTTCACATGGAA 3’
Ms_*Ifit1*_Reverse	IDT	5’ GTGCATCCCCAATGGGTTCT 3’
Ms_*Ifi44*_Forward	IDT	5’ AACTGACTGCTCGCAATAATGT 3’
Ms_*Ifi44*_Reverse	IDT	5’ GTAACACAGCAATGCCTCTTGT 3’
Ms_*Ifi44l*_Forward	IDT	5’ TGCGTGGCTTTTGTCCTACA 3’
Ms_*Ifi44l*_Reverse	IDT	5’ TTGGACATTCTGAACCTGGCT 3’
Ms_*Ifi47*_ Forward	IDT	5’ TCTCCAGAAACCCTCACTGGT 3’
Ms_*Ifi47*_Reverse	IDT	5’ TCAGCGGATTCATCTGCTTCG 3’
Ms_*Gapdh*_Forward	IDT	5’CCCCAGCAAGGACACTGAGCAAGAG3’
Ms_*Gapdh*_Reverse	IDT	5’ GGCCCCTCCTGTTATTATGGGGGT 3’
Hs_*IRF1*_Forward	IDT	5’ CAACTTCCAGGTGTCACCCA 3’
Hs_*IRF*1_Reverse	IDT	5’ CGACTGCTCCAAGAGCTTCA 3’
Hs_*IFI6*_Forward	IDT	5’ GCGGGTAAGGATGCAGGTAAG 3’
Hs_*IFI6*_Reverse	IDT	5’ ATTCAGGATCGCAGACCAGC 3’
Hs_*IFI27*_Forward	IDT	5’ CTCCTTCTTTGGGTCTGGCT 3’
Hs_*IFI27*_Reverse	IDT	5’ GGCCACAACTCCTCCAATCA 3’
Hs_*TCF7L2*_Forward	IDT	5’ GTTTGGAAGAAGCGGCCAAG 3’
Hs_*TCF7L2*_Reverse	IDT	5’ AGACAATGTGTGCCGGTGAT 3’
Hs_*LRP5*_Forward	IDT	5’ TCCCACCAAGGGCTACATCT 3’
Hs_*LRP5*_Reverse	IDT	5’ TCATGTTGGTGTCCAGGTCG 3’
Hs_*CTNNBIP1*_Forward	IDT	5’ TTGACAACGGTGACAGCACT 3’
Hs_ *CTNNBIP1*_Reverse	IDT	5’ CTCTGGGGACTCCTGCTTCT 3’
Hs_*GAPDH*_Forward	IDT	5’ AACGACCCCTTCATTGAC 3’

Author Manuscript

Author Manuscript

Author Manuscript

Author Manuscript

REAGENT or RESOURCE	SOURCE	IDENTIFIER
Hs_*GAPDH*_Reverse	IDT	5’ TCCACGACATACTCAGCAC 3’
Software and Algorithms		
Fiji	N/A	https://www.imagej.net/Fiji
Imaris 8.1 (Matlab plugin Sortomato)	Bitplane	N/A
CellProfiler	https://cellprofiler.org	Version 4.2.1
FlowJo	FLOWJO LLC	https://www.flowjo.com/
GraphPad Prism v8.3.0	GraphPad Software	https://www.graphpad.com/scientific-software/prism/
CellRanger version 3.0.2	10X Genomics	https://www.support.10xgenomics.com/single-cell-gene-expression/software/pipelines/latest/installation
R	https://www.r-project.org	Version 4.1.1
RStudio	https://www.rstudio.com	2021.09.0 Build 351
Seurat R Package (v3)	(Butler et al., 2018)	https://satijalab.org/seurat/
NicheNet	(Browaeys et al., 2018)	https://github.com/saeyslab/nichenetr
Ingenuity Pathway Analysis (IPA)	QIAGEN	https://www.qiagen.com/